

ARTICLE

DOI: 10.1038/s41467-018-07665-1

OPEN

Three-dimensional atomic scale electron density reconstruction of octahedral tilt epitaxy in functional perovskites

Yakun Yuan^{1,2}, Yanfu Lu^{1,2}, Greg Stone^{1,2}, Ke Wang², Charles M. Brooks³, Darrell G. Schlom^{3,4}, Susan B. Sinnott^{1,2}, Hua Zhou⁵ & Venkatraman Gopalan^{1,2,6}

Octahedral tilts are the most ubiquitous distortions in perovskite-related structures that can dramatically influence ferroelectric, magnetic, and electronic properties; yet the paradigm of tilt epitaxy in thin films is barely explored. Non-destructively characterizing such epitaxy in three-dimensions for low symmetry complex tilt systems composed of light anions is a formidable challenge. Here we demonstrate that the interfacial tilt epitaxy can transform ultrathin calcium titanate, a non-polar earth-abundant mineral, into high-temperature polar oxides that last above 900 K. The comprehensive picture of octahedral tilts and polar distortions is revealed by reconstructing the three-dimensional electron density maps across film-substrate interfaces with atomic resolution using coherent Bragg rod analysis. The results are complemented with aberration-corrected transmission electron microscopy, film superstructure reflections, and are in excellent agreement with density functional theory. The study could serve as a broader template for non-destructive, three-dimensional atomic resolution probing of complex low symmetry functional interfaces.

¹Department of Materials Science and Engineering, Pennsylvania State University, University Park, PA 16802, USA. ²Materials Research Institute, Pennsylvania State University, University Park, PA 16802, USA. ³Department of Materials Science and Engineering, Cornell University, Ithaca, NY 14853, USA. ⁴Kavli Institute at Cornell for Nanoscale Science, Ithaca, NY 14853, USA. ⁵Advanced Photon Source, Argonne National Laboratory, Lemont, IL 60439, USA. ⁶Department of Physics, Pennsylvania State University, University Park, PA 16802, USA. Correspondence and requests for materials should be addressed to H.Z. (email: hzhou@aps.anl.gov) or to V.G. (email: vxg8@psu.edu)

Complex oxides interfaces have become a vibrant research focus in condensed matter physics and material science^{1–5}, since they are a fertile playground for emergent phenomena such as, magnetism⁶, ferroelectricity⁷, interface charge transfer⁸, two-dimensional free electron gases⁹, superconductivity¹⁰, and topological states¹¹ through strategies in modern materials design, including strain tuning^{12–14}, artificial layering^{15,16}, spatial confinement¹⁷, and interfacial coupling^{18–25}. Control of octahedra tilts in complex oxides via film-substrate interface design, or tilt epitaxy, has been predicted to be a powerful knob for tuning various functional properties, including inversion symmetry breaking^{26–28}, magnetism^{18,22,29}, and electronic orders³⁰. Although the tilt epitaxy promises a potentially wonderful route for designing these functionalities in various materials, the experimental reports on realizing tilt epitaxy are still very limited. So far, the tilt epitaxy has been used to stabilize polar distortions in metallic ultrathin nickelates films²⁰ and to manipulate magnetic anisotropy in SrRuO₃^{18,29} and La_{2/3}Sr_{1/3}MnO₃²². However, in these works, only in-phase octahedra tilt along one of the three crystallographic axes are experimentally resolvable. Moreover, strain and substrate termination effects can convolute with tilt epitaxy, which remain unexplored.

In general, there are three outstanding challenges in implementing tilt epitaxy. The first is that substrate tilts can transfer into the film only to within ~10 unit cells, thus necessitating ultrathin films to observe these dramatic effects. Secondly, experimentally determining the complete three-dimensional (3D) structure of such tilt epitaxy interfaces with atomic resolution is quite a formidable task. Direct aberration-corrected scanning transmission electron microscopy (STEM) is now routinely used for probing atomic structures with picometers metrology; however, they probe the potential of two-dimensional projections of atomic columns, and deconvolving the information along depth direction is a challenge²², as we illustrate in this work. Coherent Bragg rods analysis (COBRA)^{31–41}, which reconstructs 3D electron density with atomic resolution based on a phase retrieval algorithm taking advantage of the interference between the diffracted X-ray beams from the thin film and the substrate, is a promising technique for such purpose. COBRA requires no special sample preparation (such as in STEM) and is readily applicable to any epitaxial system with film thickness <20 nm. However, previous COBRA studies have mostly focused on systems with high symmetry, e.g., *4mm* point group, and heavy cations. The complete 3D analysis of oxygen octahedra for a low symmetry system is still an outstanding challenge. Other emerging 3D imaging techniques (see Supplementary Table 1) include coherent diffraction imaging⁴², tomography⁴³, topography⁴⁴, ankylography⁴⁵ using X-ray or electrons, each with its own merits and drawbacks. The third challenge is to be able to deconvolve the influence of the tilt epitaxy from that of strain and surface termination effects that may coexist.

In this work, we tackle all three of these outstanding challenges. We study ultrathin films of a prototypical perovskite with a complex tilt pattern, namely calcium titanate on various substrates that provide a range of tilt and strain states. We report the atomic scale 3D reconstruction of the electron density across these low symmetry epitaxial complex oxides interfaces by COBRA, the first such feat where both substrate and film possess three octahedral tilts in addition to polar distortions. The reconstruction requires high quality mapping of diffractions in a large reciprocal space volume and generalized computer routines for handling the large experimental data set. Specifically, we present COBRA reconstructed electron densities (EDs) of ultrathin epitaxial CaTiO₃ films on NdGaO₃(110)_{or} and DyScO₃(110) and La_{0.29}Sr_{0.71}Al_{0.65}Ta_{0.35}O₃(001) (LSAT) substrates, each offering a unique combination of strain and octahedral tilt patterns across

the interface. Combining COBRA studies with complementary scanning transmission electron microscopy (STEM) and density functional theory (DFT) reveals the distinct roles of tilt epitaxy, strain and surface termination. We find that, in addition to epitaxial strain effect inducing polar distortion in the film, the tilt epitaxy monoclinically distorts the film and clamps the in-plane oxygen octahedral tilts of CaTiO₃ on LSAT substrate, giving rise to significantly higher polar transition temperatures (>900 K) in ultrathin CaTiO₃ films (8 u.c. or ~3.0 nm thick) than previously reported for thicker films (>10 nm)^{46–49}. Moreover, an unexpected out-of-plane polarization is observed in tensile strained CaTiO₃ thin films with directions dictated by the interfacial valence mismatch. These tilt epitaxy as well as valence mismatch effects should be present in all epitaxial complex oxides systems and strongly mediate the properties of ultrathin epitaxial films, which provide new routes to artificially control materials functionalities.

Results

Interplay of strain and octahedral tilts at the interface. CaTiO₃ has a centrosymmetric *Pnma* space group and is comprised of corner-shared oxygen octahedral network with interstices filled by calcium and titanium atoms. In bulk form, the oxygen octahedra exhibit out-of-phase oxygen octahedra tilts of 9.1°(*a*⁻) about the [100]_{pc} and the [001]_{pc} axes (pc: pseudocubic), and an in-phase (*b*⁺) tilt of 9.2° about the [010]_{pc} axis, denoted as *a*⁻*b*⁺*a*⁻ using the Glazer notation^{50,51}. Previous literatures using STEM imaging and dielectric measurements on 10 nm or thicker biaxially strained epitaxial CaTiO₃ films on different substrates have shown that a paraelectric to ferroelectric phase transition occurs with a tensile strain of >1.1%, leading to an in-plane polarization^{46–49}. However, we find that the story changes dramatically for ultrathin (8 u.c. or ~3.0 nm) films used in this study, where out-of-plane polarization also arises, Curie temperatures are significantly higher, the effect of chemical termination at the interface and geometric oxygen octahedral tilt mismatch between substrate and CaTiO₃ becomes important. To ascertain the above effects, an 8 u.c. of CaTiO₃ was epitaxially grown on NdGaO₃(110)_{or} (or: orthorhombic), DyScO₃(110)_{or} and LSAT(001)_{pc} substrates, with a tensile strain of 1.1%, 3.3% and 1.2%, respectively, by using Molecular Beam Epitaxy (see Methods). Similar to CaTiO₃, NdGaO₃ and DyScO₃ possess *a*⁻*b*⁺*a*⁻ tilt pattern, with out-of-phase tilts (*a*⁻) of 10.3° and 15.0°, respectively, and in-phase tilts (*b*⁺) of 9.8° and 13.0°, respectively. LSAT adopts a simple cubic structure with 0° tilts (or *a*⁰*a*⁰*a*⁰ under Glazer notation). The abrupt tilt mismatch in octahedral tilt angles across the interfaces are schematically displayed in Fig. 1a, b, where NdGaO₃ and DyScO₃ prefer enhanced angles along [100]_{pc} and [010]_{pc} axes (Fig. 1a), while LSAT tends to suppress those angles (Fig. 1b).

The 3D structures of the above systems were investigated using the COBRA method by modeling the interference between diffractions from ultrathin epitaxial CaTiO₃ films and the three substrates. As shown in Fig. 1c, the synchrotron X-ray diffraction from such epitaxial system form crystal truncation rods (CTRs) at integer *H*, *K* values (in-plane directions of the film) with a continuous distribution along the *L* (thickness direction of the film) in the reciprocal space. By rotating the sample about its surface normal (*L*) axis, the CTRs intersect with the Ewald sphere at different *L* positions, and the diffraction in the full reciprocal space can be mapped out. Measurements on CaTiO₃/NdGaO₃, CaTiO₃/DyScO₃ and CaTiO₃/LSAT were performed at both room temperature and 30 K (at which all films are in polar state). A phase-retrieval algorithm (COBRA) is then employed to reconstruct the 3D electron density in real space^{31–41} (See Methods and Supplementary Note 1 for experimental details).

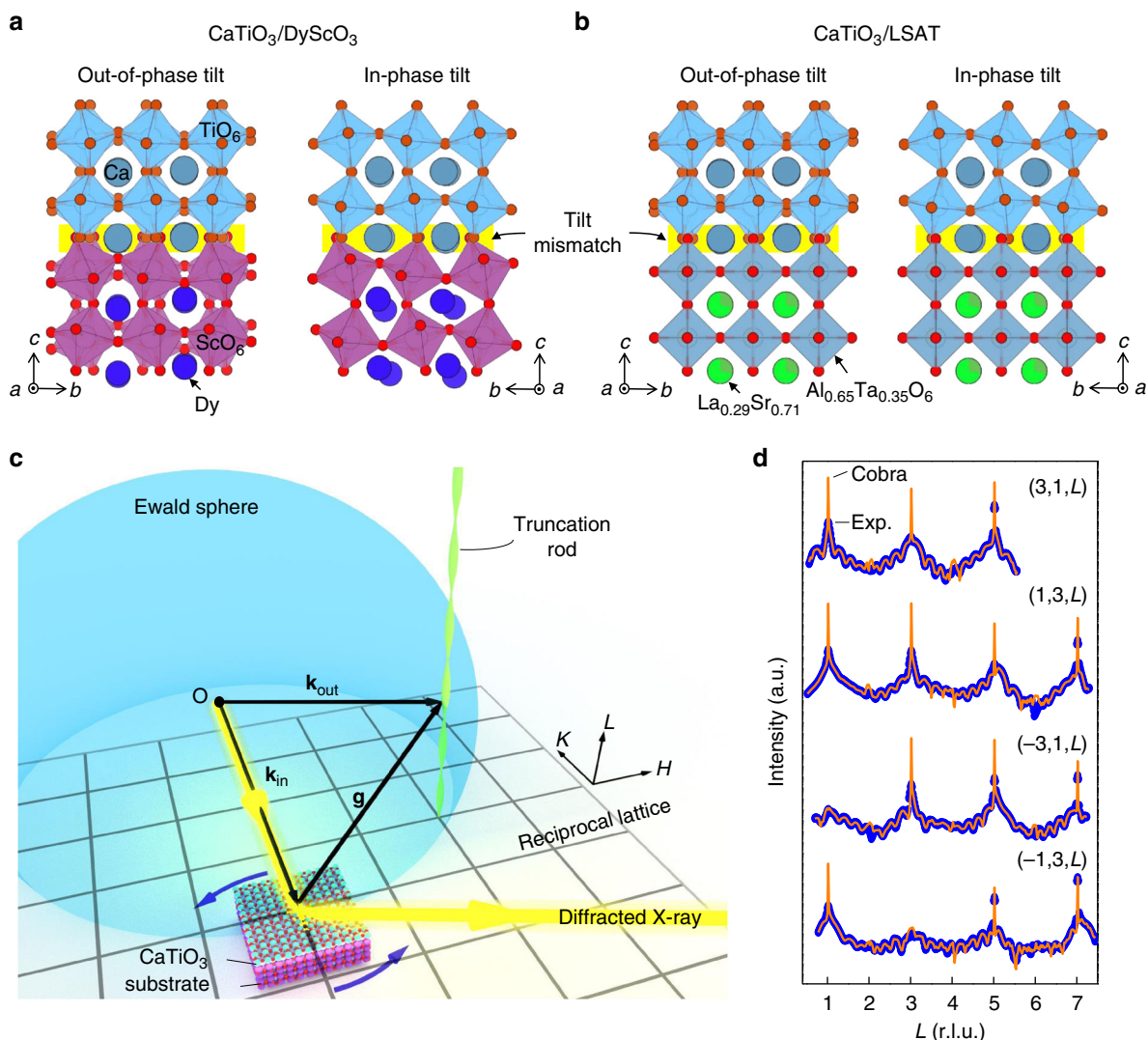


Fig. 1 The schematics of film systems and CTRs measurement. Schematic of tilt mismatch across CaTiO₃ and substrate interfaces for **a** CaTiO₃/DyScO₃ **b** CaTiO₃/LSAT. The yellow highlighted area represents the abrupt mismatch in in-plane oxygen octahedra tilt angles. **c** Experimental geometry of synchrotron X-ray diffraction used in the coherent Bragg rods analysis (COBRA) is schematically shown. The diffraction intensities along crystal truncation rods (CTRs) are mapped out by varying their intersect positions with Ewald sphere through rotating the sample about its surface normal. (H, K, L) is the coordinates in reciprocal lattice. **d** Several examples of measured crystal truncation rods, labeled as (H, K, L), where the intensity versus the reciprocal vector L is shown (blue dots) for CaTiO₃/NdGaO₃ at room temperature, as well as the corresponding COBRA fits (orange solid lines). The reciprocal units are under $2 \times 2 \times 2$ pseudocubic notation. Note that for COBRA, the substrate Bragg peaks intensities (the trees) are not as important as the diffraction structure between the peaks (the forest floor)

Figure 1d displays typical COBRA fits (orange solid lines) to experimental CTRs (blue dots) measured on CaTiO₃/NdGaO₃ at room temperature.

3D atomic structure by COBRA and DFT. The reconstructed 3D electron density maps at 30 K for CaTiO₃/NdGaO₃, CaTiO₃/DyScO₃ and CaTiO₃/LSAT are shown respectively in Fig. 2a–c. All the atomic positions, including oxygen atoms, are clearly visible as discrete peaks in the electron density maps. The high quality of the electron densities suggests the films are epitaxial and of high crystallinity. We first focus on the domain states of the three systems. Since both NdGaO₃ and DyScO₃ have the same space group ($Pnma$) as CaTiO₃, the epitaxially grown 8 u.c. CaTiO₃ is expected to follow the crystallographic orientation of substrates to minimize the interfacial energy. Indeed, a mono-domain of 8 u.c. CaTiO₃ on NdGaO₃ and DyScO₃ is

confirmed by the symmetry exhibited in CTRs (See Supplementary Note 2), as well as the consistent oxygen octahedral tilt pattern ($a^-b^+c^-$) across the interfaces, as seen in Fig. 2a, b. However, since LSAT possesses an effectively higher (cubic) symmetry ($Fm\bar{3}m$) than CaTiO₃, four symmetry equivalent domains exist within the X-ray probe area ($\sim 500 \mu\text{m}$) with equivalent fractions, as evidenced by the symmetry of the measured CTRs (See Supplementary Note 2). Therefore, the reconstructed electron densities of CaTiO₃/LSAT contains folded structural information, as shown in Fig. 2c, which is the result of spatially translating CaTiO₃ into a single pseudocubic unit cell⁵². A mixed tilt pattern of $a^-b^+c^-/a^+b^-c^-$ is observed for CaTiO₃ on LSAT. (See Supplementary Note 3 for details on structural folding and tilt pattern) The structural details of the three systems can be better visualized by breaking down the 3D electron densities into different slices of atomic planes. The ac , bc , and ab slices through the TiO₂ atomic planes of CaTiO₃/NdGaO₃ are

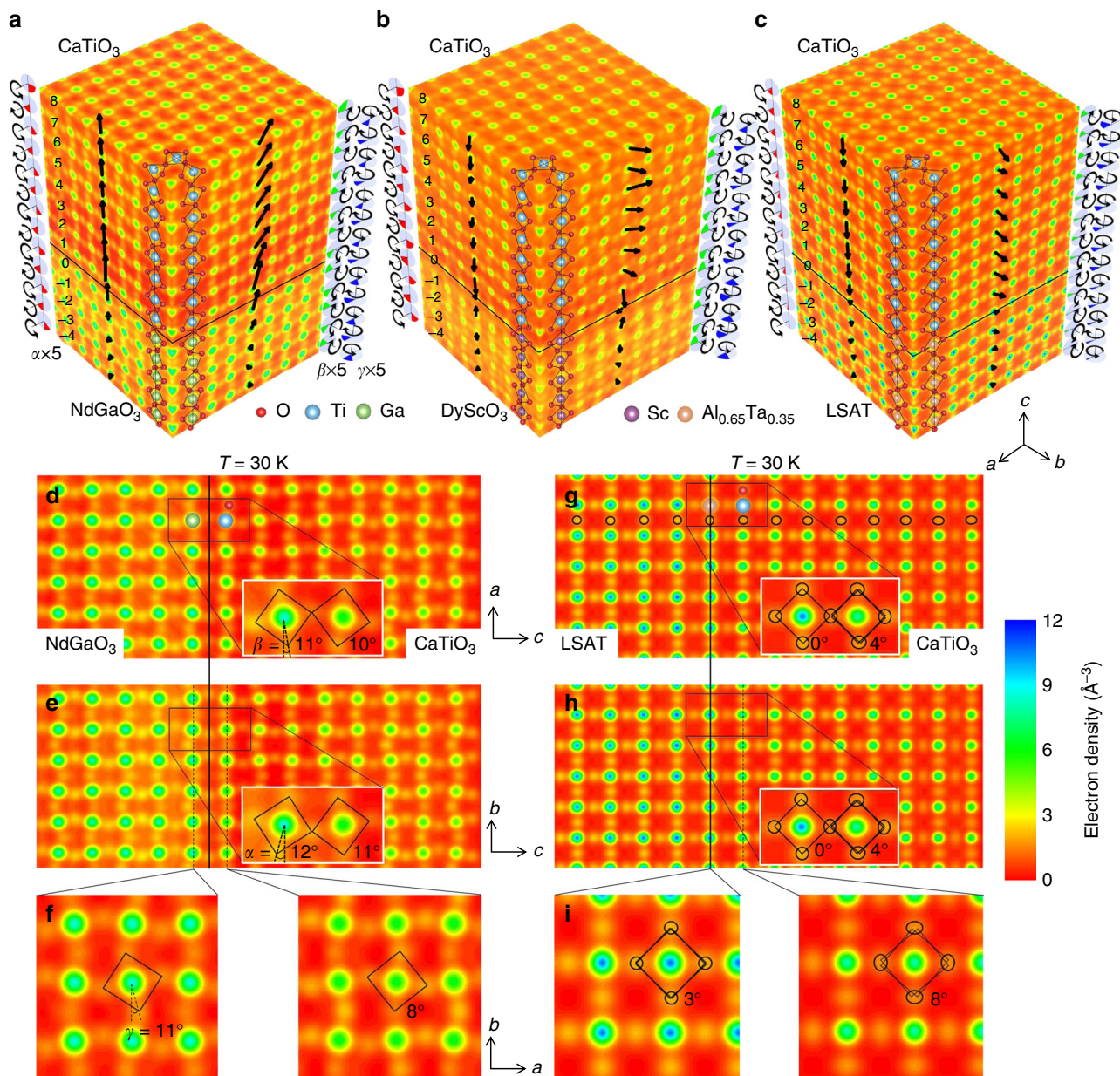


Fig. 2 3D electron densities reconstructed by COBRA at 30 K. Three-dimensional electron densities for **a** CaTiO₃/NdGaO₃, **b** CaTiO₃/DyScO₃, **c** CaTiO₃/LSAT at 30 K reconstructed by coherent Bragg rods analysis (COBRA). Polarizations projections on *ac* and *bc* planes are displayed on corresponding faces. Oxygen octahedra tilts evolution, α , β , and γ , are magnified by 5 times and displayed by red, green, and blue pie charts along each edge of electron densities. One of the four equivalent CaTiO₃ domains on LSAT are plotted for convenience of comparison. Two-dimensional slices of **d ac**, **e bc**, and **f ab** planes for CaTiO₃/NdGaO₃ and the corresponding plots **g, h, i**, for CaTiO₃/LSAT are shown, respectively. The interconnected oxygen networks are sketched by black squares, which tends to clamp the in-plane tilts (α and β) in CaTiO₃ through interface. While, the γ tilt in CaTiO₃ is unaffected

respectively displayed in Fig. 2d–f. The interconnected oxygen octahedra networks can be clearly seen in all three slices, as sketched by black squares. The tilt angles of the oxygen octahedra, α , β , and γ , are indicated on each slice. Here we focus on the impact of tilt mismatch on those angles across the interface. The β angle of the rightmost GaO₂ layer in *ac* slice is about $11 \pm 1^\circ$, while its neighboring TiO₂ layer next to the interface developed a tilt of $10 \pm 1^\circ$, which is close to the value of NdGaO₃ substrate and slightly larger than that of bulk CaTiO₃. Similar behavior is also observed in *bc* slice, where α angles of $12 \pm 1^\circ$ and $11 \pm 1^\circ$ are measured for neighboring GaO₂ and TiO₂ layers across the interface. This suggests that the interconnected octahedra network in *ac* and *bc* slices can effectively propagate the in-plane tilts (α and β) of substrate into the epitaxial film. However, with this

picture of tilt epitaxy, one would expect the out-of-plane γ tilt to be relatively decoupled across the interface. Indeed, as shown in Fig. 2f, the GaO₂ and TiO₂ layers near the interface give γ angles of $11 \pm 1^\circ$ and $8 \pm 1^\circ$, showing a relatively large change. CaTiO₃ on DyScO₃ possesses very similar structural characteristics as on NdGaO₃, where the exact same behavior can be observed; thus it is not shown here. The slices of folded 3D electron density for CaTiO₃/LSAT are shown in Fig. 2g–i. As discussed in Supplementary Note 3, the tilts of the oxygen octahedra will give rise to broadened oxygen peaks, representing multiple equivalent oxygen atom positions at corresponding oxygen sites. The broadening of oxygen peaks is indicated by the solid ellipses, which mark the contours of oxygen peaks. In this case, the tilt angles can be extracted by fitting the splitting of the oxygen atoms at each site.

The *ac* slice in Fig. 2g shows an increase of ellipticity of oxygen peaks from the interface to the surface of the film, indicating an increase of tilt angles. The *bc* slice (Fig. 2h) shows the same behavior due to the symmetry equivalency of *a* and *b* axes of the folded electron density. The in-plane tilt angles (α and β) for the neighboring $\text{Al}_{0.65}\text{Ta}_{0.35}\text{O}_2$ and TiO_2 layers are respectively $0 \pm 2^\circ$ and $4 \pm 2^\circ$, yielding significantly smaller in-plane tilt magnitudes in CaTiO_3 film compared to its bulk values. This again agrees with the tilt epitaxy effect through the interface. Similarly, the γ angles are $4 \pm 3^\circ$ for $\text{Al}_{0.65}\text{Ta}_{0.35}\text{O}_2$ and $8 \pm 3^\circ$ for TiO_2 layers near the interface, confirming that the γ tilt of the CaTiO_3 film is decoupled from the substrate.

Quantitative analysis of the 3D electron densities is performed as follows. By fitting each peak in the electron density with 3D Gaussian functions, the 3D coordinates of atoms in each unit cell from 5 u.c. beneath the substrate to the surface of the 8 u.c. thick film are extracted. Electrical polarization vectors are calculated by using cations displacements relative to anions (oxygen) and their nominal charges. The projections of polarization vectors on *ac* and *bc* planes are plotted as black arrows on the corresponding faces of the electron density maps (Fig. 2a–c), depicting a polar phase at 30 K in films on all three substrates. For convenience of comparison, one of the four equivalent domains on LSAT is plotted.

The polarizations vector evolution along the growth direction is discussed next. As illustrated in Fig. 3a–c, CaTiO_3 films on DyScO_3 , NdGaO_3 , and LSAT, respectively exhibit average in-plane polarizations of -20.6 ± 2.1 , -14.9 ± 1.8 , and $13.5 \pm 2.5 \mu\text{Ccm}^{-2}$ along the *a*-axis (green circles). There is no measurable polarization along the *b*-axis (blue circles). The magnitudes of the in-plane polarizations qualitatively agree with the larger tensile strain states on DyScO_3 (3.3%) and smaller tensile strain on NdGaO_3 (1.1%) and LSAT (1.2%); the numbers however deviate from previous theory predictions on bulk state⁴⁷, which will be addressed in detail further on. Most interestingly, unexpected out-of-plane polarization components are observed in CaTiO_3 on all three substrates (red circles in Fig. 3a–c).

Remarkably, COBRA indicates that the directions of the out-of-plane polarizations appear to be dictated by the substrate terminations, due to a valence mismatch effect²¹. The NdO layer termination of NdGaO_3 substrate, as indicated by the black line in Fig. 2a, with a valence mismatch of +1, prefers an out-of-plane polarization towards the +*c* direction. In contrast, electron density in Fig. 2b, c (black lines) indicate that an ScO_2 and $\text{Al}_{0.65}\text{Ta}_{0.35}\text{O}_2$ (BO_2) termination with a valence mismatch of -1 and -0.3, respectively, result in an out-of-plane polarization direction of -*c*. These COBRA reconstructed surface terminations are confirmed experimentally using transmission electron microscopy as shown in Supplementary Figure 5.

The combination of in-plane and out-of-plane polarization components determine the polarization vectors as shown, which lie in a single mirror plane, indicating the monoclinic symmetry with *m* in the *ac* plane. Note that to reveal this low symmetry distortion by COBRA, one has to collect enough truncation rods; in this particular case, up to 47 CTRs for each system were collected. Further, in contrast to previous COBRA algorithm, the current phase retrieval algorithm was generalized to include all possible crystallographic symmetries.

Quantitative structural analysis of the oxygen octahedral tilt angles α , β , and γ , respectively about the *a*, *b* and *c* axes, are performed by analyzing oxygen atom peaks in each BO_6 octahedron and are depicted as pie charts along the edges of the electron density maps (Fig. 2a–c) as well as plotted in Fig. 3d–f as green (α), blue (β), and red (γ) circles. COBRA reveals a gradual change in the α and β values and a relatively drastic change in the γ values across the interfaces for all three

systems, as suggested by the 2D slices in Fig. 2d–i. This is expected due to the tilt epitaxy effect on the α and β angles between the substrates and their corresponding CaTiO_3 films through the shared interfacial oxygen atoms (as illustrated in Fig. 1a, b), while the γ angles are not affected, allowing for a drastic change across the interface.

The above reconstructed 3D oxygen tilts and polar displacements in the film suggest the role of substrate strain, substrate oxygen octahedral tilts, and substrate terminations. To understand and deconvolve these effects, density functional theory (DFT) calculations were performed (see Methods). The DFT results for the three components of the polarization and the octahedral tilts for each film system are plotted using solid lines in Fig. 3a–f, showing excellent agreement between the calculations and COBRA experiments. To uncouple the changes in the octahedral tilts induced by tilt epitaxy from the changes due to a pure biaxial strain, bulk calculations on strained CaTiO_3 (with no interfaces) were performed. The differences in the magnitude of in-plane octahedral tilts, $|\Delta\alpha| + |\Delta\beta|$, between the film and the substrate were smaller in the case where the tilt epitaxy effect is present versus when the substrate simply imparts a biaxial strain. (See Supplementary Table 2 for summary of tilt angles) For example, for the $\text{CaTiO}_3/\text{NdGaO}_3$ film system, $|\Delta\alpha| + |\Delta\beta| = 0.63^\circ$ from DFT which agrees well with the measured $0.7 \pm 0.5^\circ$ from the COBRA reconstruction. In contrast, it is 1.21° from the strained bulk calculation where there is no interface tilt epitaxy effect, thus indicating the important role of tilt epitaxy in minimizing the in-plane tilts difference ($|\Delta\alpha| + |\Delta\beta|$) across the interface. A similar trend for $|\Delta\alpha| + |\Delta\beta|$ is seen for the other two film systems: 6.33° (DFT including tilt epitaxy) and $3.7 \pm 1.3^\circ$ (COBRA) versus 8.5° (DFT bulk without tilt epitaxy) for the $\text{CaTiO}_3/\text{DyScO}_3$; and respectively, 8.58° and $12.7 \pm 1.0^\circ$ versus 18.88° for the $\text{CaTiO}_3/\text{LSAT}$ system. These qualitatively excellent and quantitatively good comparisons between DFT and COBRA confirm the tilt epitaxy and valence mismatch effects on the in-plane and out-of-plane polarization components of epitaxial CaTiO_3 thin films.

Interface controlled polarization state. The influence of interfacial tilt epitaxy and valence mismatch effects is expected to diminish as the epitaxial film thickness increases and should be much more prominent in ultrathin films. Fig. 3g, h show the polarization comparison between literature values on thick CaTiO_3 films ($>10 \text{ nm}$)^{46–49} and values on ultrathin films studied in this work, where theoretical phase field simulations (green lines), DFT (yellow lines) on strained bulk CaTiO_3 , dielectric measurement results on $>10 \text{ nm}$ thick CaTiO_3 films (green squares, blue triangles), as well as COBRA (open stars) and DFT (closed stars) results on ultrathin (8 and 6 u.c., respectively) epitaxial CaTiO_3 films are presented. The comparison of in-plane polarization (Fig. 3g) shows a perfect match between experimentally measured polarization on thick CaTiO_3 films (green squares and blue triangles) and theoretical calculation (green and yellow lines) on strained bulk CaTiO_3 , where no interface is present. DFT calculations (closed stars) on ultrathin epitaxial CaTiO_3 films agree well with COBRA results (open stars). The slight increase in the in-plane polarization at 3.3% strain for ultrathin films is consistent with the fact that higher tensile strain favors larger in-plane polarization. The ultrathin films give significantly higher in-plane polarization under 1.1–1.2% strain (NdGaO_3 and LSAT) and lower polarization under 3.3% strain (DyScO_3) as compared to thick films, which suggests that the interfacial tilt epitaxy effect can dominate the properties of these films. Similarly, in Fig. 3h, tensile strained bulk CaTiO_3 exhibits zero out-of-plane polarization components, while ultrathin films show a clear non-zero

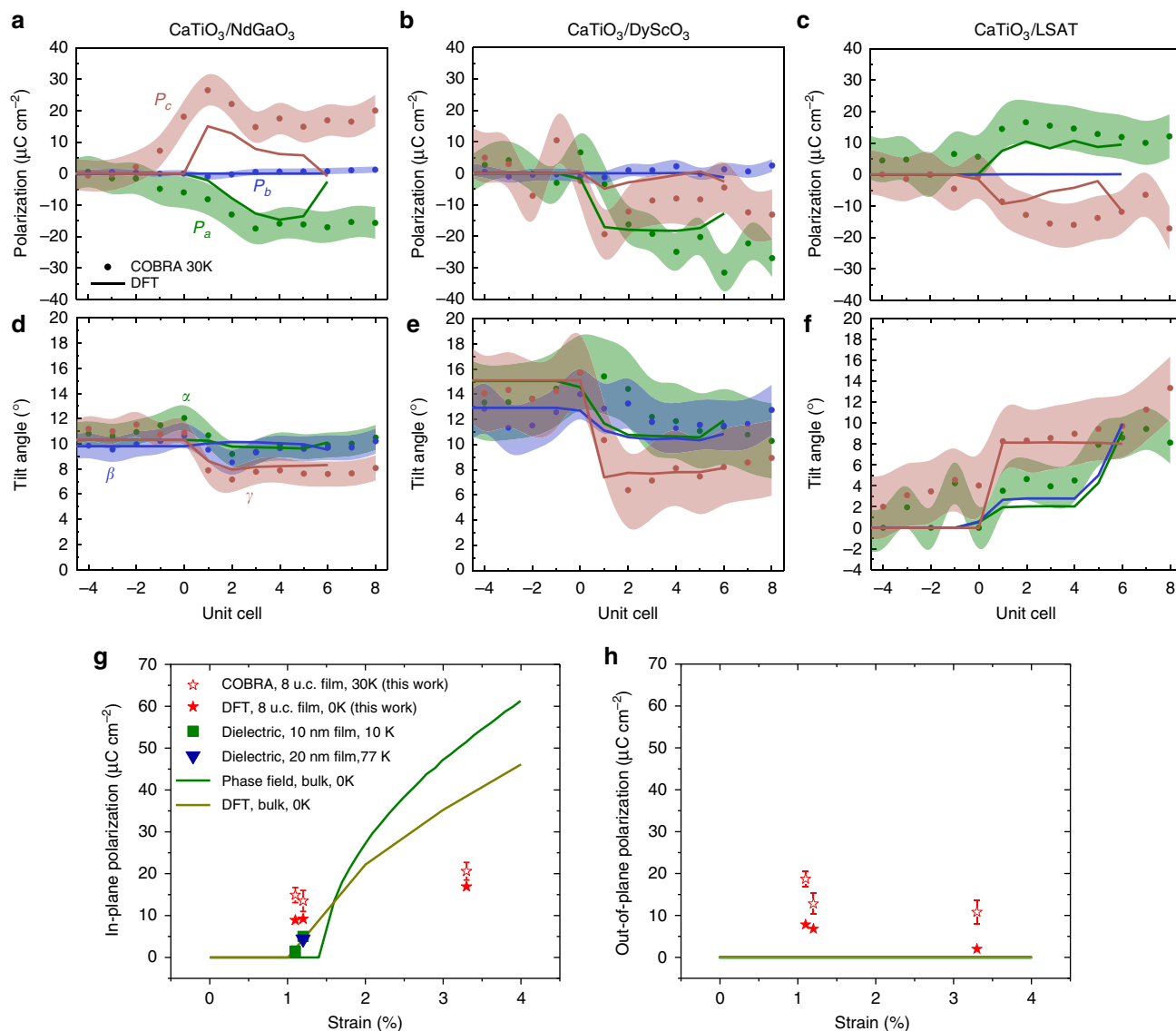


Fig. 3 Tilt angles and polarizations in ultrathin CaTiO_3 films. **a-c** Polarization components, P_a (green), P_b (blue), and P_c (red), as well as **d-f** quantified tilt angles, α (green), β (blue), and γ (red), extracted from coherent Bragg rods analysis (COBRA) (dots) and density functional theory (DFT) (solid lines) are compared for the films on NdGaO_3 , DyScO_3 , and LSAT . The experimental errors are estimated by comparing COBRA results for substrates to their bulk reference values and are indicated by the shaded area surrounding the COBRA data dots. **g** The polarization state of ultrathin CaTiO_3 are compared to literature reports on thick samples (>10 nm). Theoretical works by phase field simulation (green line⁴⁷) and DFT (yellow line⁴⁶) were performed on bulk CaTiO_3 at 0 K. Experimental works on epitaxial thin film were measured by low temperature dielectric measurements. Green squares show measurements on 10 nm CaTiO_3 at 10 K⁴⁹. Blue triangle shows measurement on 20 nm CaTiO_3 at 77 K⁴⁸. The in-plane polarizations obtained by COBRA method at 30 K for 8 u.c. films and DFT for 6 u.c. films are respectively plotted using red open and closed stars. **h** Phase field (green line) and DFT (yellow line) show no out-of-plane polarization for strained bulk CaTiO_3 . COBRA (red open star) and DFT (red closed star) reveal a clear non-zero out-of-plane polarization in ultrathin CaTiO_3 films

polarization with decreased magnitude at 3.3% tensile strain. This non-zero polarization in ultrathin films again display the effect of interfacial tilt epitaxy and its competition with strain. We also notice that the tilt angles of these ultrathin films change significantly over the first few unit cells, and then tend to relax on approaching the surfaces; however, they do not fully relax to the bulk value within the 8 u.c. This explains the reduced out-of-plane polarization on approaching the film surface. (The outermost u.c. has surface effects and is not included in the discussion here.) With the tilt epitaxy being the driving force, the long-range electrostatic interaction also plays a role in stabilizing this out-of-plane polarization state. The larger out-of-plane polarization in the first few layers favors the polarization with the same direction

in the rest of the film, while a depolarization field leads to the relaxation of the out-of-plane polarization from the interface to the film surface.

Probing tilt epitaxy by STEM. Aberration-corrected scanning transmission electron microscopy (AC-STEM) was also employed to confirm the structure determined from COBRA reconstruction at room temperature, to the extent possible by STEM. Atomic resolution annular bright field scanning transmission electron microscopy (ABF-STEM) of the above three epitaxial systems along $[010]_{\text{pc}}$ (b -axis) zone axis reveal high quality CaTiO_3 thin films that are epitaxially grown on three different substrates, as

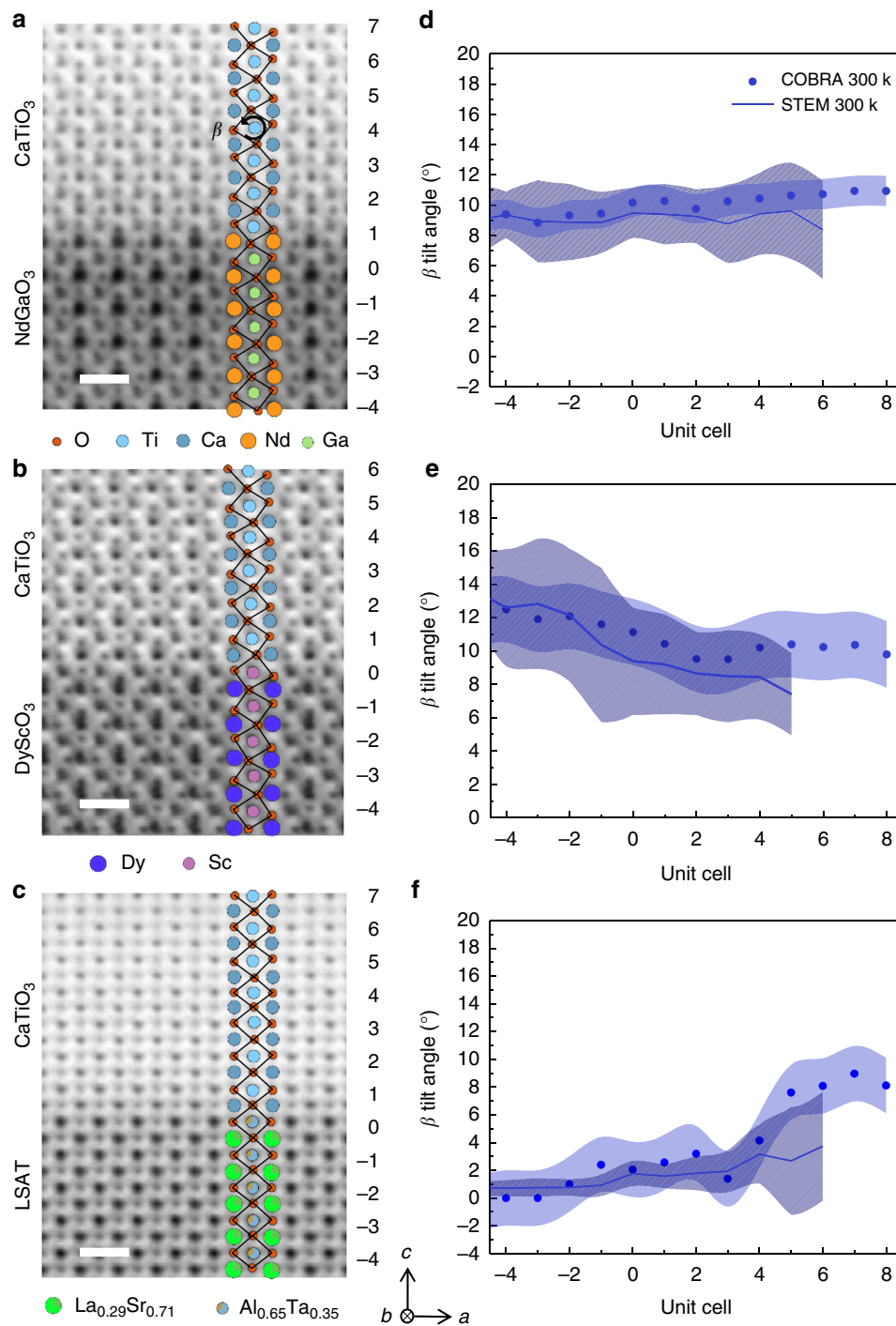


Fig. 4 Room temperature evolution of β angles across interfaces. High resolution annular bright field scanning transmission electron microscopy (ABF-STEM) images with oxygen atoms at room temperature for **a** CaTiO₃/NdGaO₃, **b** CaTiO₃/DyScO₃, **c** CaTiO₃/LSAT along [010]_{pc} (*b*-axis) zone axis. Different unit cells are labeled by numbers on the right side of the STEM images. The scale bar is 5 Å. The β angles (blue lines) resolved by STEM for different unit cells along *c* direction are plotted in **d**, **e**, and **f**, respectively for above systems. As comparison, room temperature coherent Bragg rods analysis (COBRA) data are plotted using blue dots. Experimental errors for STEM (line shaded area) are taken to be the standard deviation of the β values along *a*-axis over around 20 unit cells. The errors for COBRA data (light blue shaded area) are obtained by comparing substrates β values to their bulk reference

shown in Fig. 4a–c. The substrate surface termination of NdO (AO) for NdGaO₃, ScO₂ (BO₂) for DyScO₃, and Al_{0.65}Ta_{0.35}O₂ (BO₂) for LSAT are confirmed by energy dispersive spectroscopy mapping (see Supplementary Figure 5), which are in excellent agreement with the COBRA data. Oxygen atoms in all three

systems are clearly visible and display a consistent *b*⁺ tilt pattern. In Fig. 4d–f, the evolution of the β values obtained from AC-STEM (blue lines) shows a gradual change across the interfaces and are in good agreement with the analysis of room temperature electron densities reconstructed by COBRA (blue dots). Similar to

the low temperature results, a significant suppression of $\text{CaTiO}_3\beta$ values is observed on the LSAT substrate. Supplementary Note 4 shows the complete room temperature COBRA results. Since STEM probes 2D projection of atom columns, constructing 3D information relies on images along multiple zone axes. Supplementary Notes 5 and 6 show STEM analysis on $[100]_{\text{pc}}$ and $[110]_{\text{pc}}$ zone axes. While the qualitative agreement between STEM and COBRA data is reasonable, the results illustrate clearly the challenge in STEM in quantitatively determining the out-of-phase tilts α and γ angles that COBRA is easily able to do.

Probing the polar state using SHG method. To confirm the point group symmetry resolved by COBRA, and to investigate the polar transition Curie temperature (T_C), we employ optical second harmonic generation (SHG), schematically shown in Fig. 5a, where a linearly polarized light $\lambda = 800$ nm is incident onto the sample at an angle θ , and the second harmonic signal at $\lambda = 400$ nm is measured. In Fig. 5b, temperature dependent SHG signal reveals Curie temperatures T_C of 200 and 350 K, respectively, for 8 u.c. CaTiO_3 on NdGaO_3 and DyScO_3 , which are significantly higher than that of 70 and 170 K, reported in thick films (10 nm) in literatures^{47,49}. Most strikingly, CaTiO_3 on LSAT exhibits significant SHG signal from 4 up to 900 K. However, literature reports a T_C of 140–190 K for thick CaTiO_3 films (>10 nm) on LSAT^{48,49}. Room temperature electron densities reconstructed by COBRA confirm a paraelectric state for CaTiO_3 on NdGaO_3 , a weak polarization of the film on DyScO_3 and a large polarization of the film on LSAT (see Supplementary Figure 6). The large enhancement of polar transition temperature, T_C , in the 8 u.c. CaTiO_3 films in this work as compared to thicker films is a direct result of the interfacial tilt epitaxy effect, which stabilizes the polar phonon soft mode against its competing centric oxygen octahedral modes through interfacial coupling⁵³. For the same reason, 8 u.c. CaTiO_3 on LSAT exhibits the highest T_C (>900 K) among all three systems, due to its smallest tilt angles arising from the tilt epitaxy on a substrate with no tilts. Symmetry of CaTiO_3 is determined by SHG polarimetry, where s-/p-polarized SHG signal components, $I_{2\omega,s}$ and $I_{2\omega,p}$, are measured as a function of incident polarization angle φ (see Methods). Theoretical modeling (see Fig. 5c and Supplementary Fig. 10) indicates a single domain point group of m for the films on NdGaO_3 and DyScO_3 and four equivalent m domains with each domain fraction of ~ 0.25 for the film on LSAT. These results are consistent with the polar states extracted from the COBRA electron density maps.

Discussion

This work demonstrates that tilt epitaxy, namely, slight changes in octahedral tilts in perovskites through interfacial tilt control can dramatically influence the functional properties of ultrathin films. The reconstructed 3D electron density in ultrathin films clearly reveal the intertwining roles of tilt epitaxy, substrate strain, and substrate surface terminations. These give rise to unexpected out-of-plane and in-plane polarization components, as well as large enhancement of polar Curie temperatures T_C . An important highlight of this work is the development of the Fourier phase retrieval COBRA method to successfully reconstruct the 3D atomic resolution structure of low symmetry complex oxides interfaces with all independent octahedral tilts and polarization vectors in both the film and substrate, the most complex low symmetry interface structure reconstructed to date by this technique. With the development of high-energy surface X-ray diffraction⁵⁴ that enables the rapid capture of large portions of 3D Bragg rods in reciprocal space, COBRA measurements will become much more efficient and widespread in their application to oxide thin films and heterostructures. This work will motivate

progress in the fledgling field of tilt epitaxy engineering in ultrathin perovskite films, and more broadly, provide a powerful non-destructive tool with atomic resolution for probing the electron density of complex functional interfaces.

Methods

Sample growth by molecular beam epitaxy. Epitaxial CaTiO_3 thin films were grown on DyScO_3 , NdGaO_3 , and LSAT using reactive molecular-beam epitaxy (MBE) in a Veeco GEN10 system equipped with reflection high-energy electron diffraction (RHEED) and utilizing a background partial pressure of $\sim 5 \times 10^{-7}$ Torr of distilled ozone. Calcium was evaporated from an effusion cell and titanium from a Ti-Ball™ sublimation source. The fluxes of the constituent elements, calcium and titanium, were measured using a quartz crystal monitor (QCM) and typical values for each element were around 2×10^{13} atoms $\text{cm}^{-2}\text{s}^{-1}$. The 8 u.c. CaTiO_3 films were grown at a temperature of 650 °C by co-depositing CaO and TiO_2 . The starting fluxes of the Ca and Ti molecular beams were initially determined by QCM and then the calcium flux was fine-tuned to match the flux of the titanium using shuttered RHEED intensity oscillations. Due to the imperfect growth control, the exact thickness of these films is determined to be slightly larger than 8 u.c. with incomplete surface layers, as discussed in Supplementary Note 7.

Crystal truncation rods measurements and coherent Bragg rods analysis.

Crystal truncation rods (CTRs) were measured using a surface X-ray diffraction geometry with a six-circle diffractometer under X-ray photon energy of 16 and 23.9 keV at sectors 12-ID-D and 33-ID-D at Advanced Photon Source, Argonne National Laboratory. Both beamlines have a similar total flux of $\sim 2.0 \times 10^{12}$ photons s^{-1} . At 33-ID-D, the X-ray beam was focused by a pair of Kirkpatrick–Baez mirrors down to a beam profile of 50 μm (vertical) \times 500 μm (horizontal). The two-dimensional diffraction images of CTRs at each L step in the reciprocal space were recorded with a pixel array area detector (Dectris PILATUS 100 K). Samples were protected under dry helium gas flow in a concealed sample cell during room temperature measurements. Low temperature measurement was achieved with a closed-cycle-cryocooler system (Advanced Research System Model DE-204). A large set of CTRs in the reciprocal lattice coordinate were measured for all three epitaxial CaTiO_3 films at both room temperature and low temperature (30 K), with $H_{\text{max}}, K_{\text{max}} = 8$ r.l.u., $L_{\text{max}} = 9$ r.l.u. under $2 \times 2 \times 2$ pseudocubic notation.

3D electron densities (EDs) for the complete atomic structures were reconstructed from the complete set of CTRs by using an iterative phase retrieval technique, known as coherent Bragg rods analysis (COBRA)^{32,34,35,52,55}, through an in-house developed MATLAB code, generalized for systems with symmetry lower than $4mm$ (or simple four-fold symmetry system). Experimental CTR data were first background subtracted, and then properly corrected for geometric and polarization factors. Initial atomic structural model was constructed based on bulk structures with fitted CaTiO_3c lattice constant using GenX software⁵⁶. Within each iteration, real space and reciprocal space constraints are alternatively applied to reconstruct phase information from measured CTRs. The structural results yielded by the COBRA iterations are found to be insensitive to the initial model, as illustrated in Supplementary Note 8.

The generic approach for uncertainty analysis based on a parameterized model is not applicable to COBRA-generated EDs. A method called noise analysis based on statistical analysis is previously used to determine the uncertainties in COBRA results³². This method requires COBRA reconstructed EDs of a large number of groups of CTRs adding afterward with random noise and analyzes the degree of scatters in the interested values extracted from EDs, which is extremely costly for analyzing six different systems (three epitaxial structures at room temperature and 30 K) presented in this work. By taking advantages of ultrathin CaTiO_3 films and well-known substrates used in this work, we estimate the uncertainty by including 11 pseudocubic u.c. of substrates into the reconstructed EDs. The structures of substrate unit cells buried underneath the 5th u.c. away from the interfaces should maintain their bulk structures. Therefore, the deviation between EDs and bulk structures for the first 6 u.c. of substrates is used for estimating the magnitude of deviation between COBRA results and the true values. A comparison between above two methods is detailed in Supplementary Note 9.

Density functional theory calculations. The density functional theory (DFT) calculations use the plane-wave basis and projector augmented wave (PAW)⁵⁷ method within the Vienna Ab initio Simulation Package (VASP)⁵⁸. The choice of the exchange-correlational functional is the Perdew–Burke–Ernzerhoff (PBE)⁵⁹ generalized gradient functional. Convergence tests indicate that energies are converged to within 1 meV atom^{-1} with a 560 eV cutoff energy, with 20 Å of vacuum in the direction perpendicular to the interface, and with a $8 \times 8 \times 1$ k-point mesh. Spin-polarization is used in all the calculations. Structure relaxation is iterated until the energy differences are below 10^{-6} eV and until all forces on the atoms are below 0.05 eV Å⁻¹. To minimize the unphysical dipole energy arising from the heterostructure, CaTiO_3 thin films were symmetrically introduced on both side of the substrate. During the calculation, all the substrate atoms are fixed at their initial positions and are not allowed to relax.

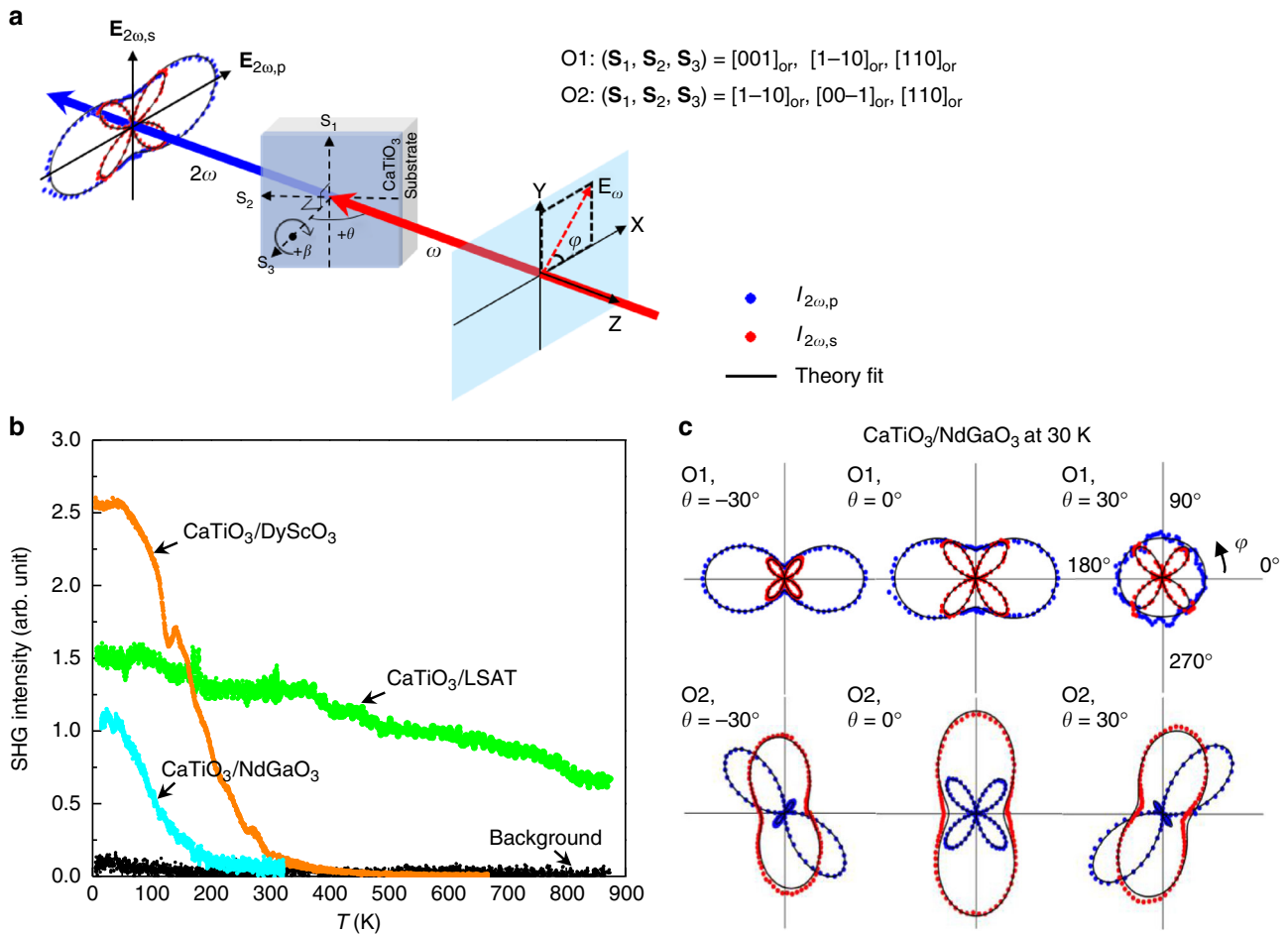


Fig. 5 SHG measurements on ultrathin CaTiO₃ films. **a** Schematic of far-field transmission optical second harmonic generation (SHG) setup. Linear polarized fundamental $\lambda = 800$ nm, with polarization direction described by φ is incident onto the sample at an angle θ . Transmitted s-/p-polarized SHG signal $\mathbf{E}_{2\omega,s}$, $\mathbf{E}_{2\omega,p}$ at $\lambda = 400$ nm is measured. **b** Temperature dependent SHG signal of CaTiO₃ on NdGaO₃, DyScO₃, and LSAT reveals Curie temperature T_C of 200, 350, and >900 K, respectively. **c** Polarimetry signal $I_{2\omega,s}$ (red dots), $I_{2\omega,p}$ (blue dots) on CaTiO₃/NdGaO₃ at 30 K are shown. Two sample orientations, O1 and O2, are experimentally measured as described by $(\mathbf{S}_1, \mathbf{S}_2, \mathbf{S}_3)$ under orthorhombic notation. Theory fits (black lines) reveals a single domain m symmetry of the CaTiO₃ on NdGaO₃ at 30 K

Scanning transmission electron microscopy imaging. The scanning transmission electron (STEM) images of CaTiO₃ thin films on NdGaO₃, DyScO₃, and LSAT under (100)_{pc}, (010)_{pc}, and (110)_{pc} zone axes were collected on an FEI Titan G2 double aberration-corrected HR-STEM at 300 kV with a probe illumination angle of 28 mrad. High-angle annular dark-field (HAADF) and annular bright field (ABF)-like images were obtained with collection angles of 42–244 and 9–51 mrad, respectively. At each sample location, images were taken with the STEM fast scan direction set to 0° and 90° with respect to the substrate interface direction. These image pairs were then drift corrected, after which the images were superimposed.

Analysis of the STEM images was performed using custom-written MATLAB code. The sub-pixel resolution of the cations and oxygen positions were determined by fitting a seven parameter 2D elliptical Gaussian profile (to account for any ellipticity in the intensity distribution) to the HAADF/ABF intensity distribution.

Optical second harmonic generation measurements. Optical second harmonic generation (SHG) polarimetry and temperature dependent measurements were performed in a far-field transmission setup using femtosecond pulses at $\lambda = 800$ nm generated by a Spectra-Physics Empower Q-switched Nd:YLF pumped Solstice Ace Ti:Sapphire laser system (100 fs, 1 kHz). The experimental schematic is shown in Fig. 5a, where a linear polarized fundamental field with polarization direction φ incident on the sample at an incident angle θ . The p-polarized ($I_{2\omega,p}$) and s-polarized ($I_{2\omega,s}$) components of second harmonic field ($\mathbf{E}_{2\omega}$) was first spectrally filtered and then detected by a photo-multiplier tube, using lock-in method (SR830). For each sample, systematic polarimetry was performed by rotating the incident polarization φ at fixed θ for two different sample orientations (O1 and O2). SHG polarimetry on CaTiO₃/NdGaO₃ at 30 K was performed at incident angles $\theta = -30^\circ, 0^\circ, 30^\circ$ for two sample orientations, O1: $(\mathbf{S}_1, \mathbf{S}_2, \mathbf{S}_3) = ([001]_{\text{or}}, [1-10]_{\text{or}}, [110]_{\text{or}})$, O2: $(\mathbf{S}_1, \mathbf{S}_2, \mathbf{S}_3) = ([1-10]_{\text{or}}, [00-1]_{\text{or}}, [110]_{\text{or}})$, as shown in Fig. 5c (red and blue dots). Similar SHG behavior are also observed in CaTiO₃/

DyScO₃ at 30 K (See Supplementary Figure 10). SHG polarimetry on CaTiO₃/LSAT with sample orientations, O1: $(\mathbf{S}_1, \mathbf{S}_2, \mathbf{S}_3) = ([100]_{\text{pc}}, [010]_{\text{pc}}, [001]_{\text{pc}})$, O2: $(\mathbf{S}_1, \mathbf{S}_2, \mathbf{S}_3) = ([010]_{\text{pc}}, [-100]_{\text{pc}}, [001]_{\text{pc}})$, reveals a similar pattern at 30 K and room temperature, as shown in Supplementary Figure 10, and is different from CaTiO₃ on NdGaO₃ and DyScO₃. Temperature-dependent measurements were performed by monitoring the SHG signal while scanning the sample temperature, which was controlled using helium cooled Janis 300 cryostat (for low temperature) and a heater (for high temperature).

Symmetry analysis of the SHG polarimetry was performed using an analytical model described below^{60,61}. Fundamental field is written as $(E_\omega \cos(\varphi), E_\omega \sin(\varphi), 0)$ under the laboratory coordinates (X, Y, Z) , and incident onto sample at an angle θ . Sample orientation can be described by β , with $\beta = 0^\circ$ for O1 and $\beta = 90^\circ$ for O2. Considering refraction and transmission at sample surface, the fundamental field $E'_{\omega,i}$ inside the sample can be expressed as

$$E'_{\omega,1} = (\cos(\theta') \cos(\beta) \cos(\varphi) t_p - \sin(\beta) \sin(\varphi) t_s) E_\omega \quad (1)$$

$$E'_{\omega,2} = (\cos(\theta') \sin(\beta) \cos(\varphi) t_p + \cos(\beta) \sin(\varphi) t_s) E_\omega \quad (2)$$

$$E'_{\omega,3} = -\sin(\theta') \cos(\varphi) t_p E_\omega \quad (3)$$

Where $\sin(\theta') = \sin(\theta)/n$, n is refractive index, and $t_p = 2\cos(\theta)/[n\cos(\theta) + \cos(\theta')]$ and $t_s = 2\cos(\theta)/[\cos(\theta) + n\cos(\theta')]$ are Fresnel coefficients. The SHG field $E'_{2\omega,i}$ generated inside the sample can be calculated by $E'_{2\omega,i} = d'_{ijk} E'_{\omega,j} E'_{\omega,k}$, d'_{ijk} is nonlinear SHG coefficients, or under Voigt notation, $E'_{2\omega,i} = d'_{ij} E'_{\omega,j}$. d'_{ij} matrix

for m point group symmetry is:

$$d^m = \begin{pmatrix} 0 & 0 & 0 & 0 & d_{15} & d_{16} \\ d_{21} & d_{22} & d_{23} & d_{24} & 0 & 0 \\ d_{31} & d_{32} & d_{33} & d_{34} & 0 & 0 \end{pmatrix} \quad (4)$$

To simplify the analysis, we ignored the dispersion effect, i.e., $n = n_\omega \approx n_{2\omega}$. The transmitted SHG field in the laboratory coordinates is:

$$E_{2\omega,p} = E_{2\omega,X} = (\cos(\theta') \cos(\beta) E'_{2\omega,1} + \cos(\theta') \sin(\beta) E'_{2\omega,2} - \sin(\theta') E'_{2\omega,3}) t'_p \quad (5)$$

$$E_{2\omega,s} = E_{2\omega,Y} = (-\sin(\beta) E'_{2\omega,1} + \cos(\beta) E'_{2\omega,2}) t'_s \quad (6)$$

Where $t'_p = 2n \cos(\theta') / [n \cos(\theta) + \cos(\theta')]$, $t'_s = 2n \cos(\theta) / [\cos(\theta) + n \cos(\theta')]$. SHG intensity from sample is $I_{2\omega,p} = \alpha |E_{2\omega,p}|^2$ and $I_{2\omega,s} = \alpha |E_{2\omega,s}|^2$, where α is a constant. In above equations, α and E_ω can be further eliminated by defining effective SHG matrices as $d_{ij}^{\text{eff}} = \sqrt{\alpha} E_\omega^2 d_{ij}$. For CaTiO₃ on NdGaO₃ and DyScO₃, single domain state of CaTiO₃ films is observed. Explicitly, we have following equations for orientations O1 and O2:

$$\text{O1} : \begin{cases} I_{2\omega,p}^{\text{total}} = I_{2\omega,p}(\beta = 0^\circ) \\ I_{2\omega,s}^{\text{total}} = I_{2\omega,s}(\beta = 0^\circ) \end{cases} \quad (7)$$

$$\text{O2} : \begin{cases} I_{2\omega,p}^{\text{total}} = I_{2\omega,p}(\beta = 90^\circ) \\ I_{2\omega,s}^{\text{total}} = I_{2\omega,s}(\beta = 90^\circ) \end{cases} \quad (8)$$

For CaTiO₃ on LSAT, four equivalent domains represented by different β values are considered. Under the phase uncorrelated approximation, we have following equations:

$$\text{O1} : \begin{cases} I_{2\omega,p}^{\text{total}} = w_1 I_{2\omega,p}(\beta = 0^\circ) + w_2 I_{2\omega,p}(\beta = 90^\circ) + w_3 I_{2\omega,p}(\beta = 180^\circ) + (1 - w_1 - w_2 - w_3) I_{2\omega,p}(\beta = 270^\circ) \\ I_{2\omega,s}^{\text{total}} = w_1 I_{2\omega,s}(\beta = 0^\circ) + w_2 I_{2\omega,s}(\beta = 90^\circ) + w_3 I_{2\omega,s}(\beta = 180^\circ) + (1 - w_1 - w_2 - w_3) I_{2\omega,s}(\beta = 270^\circ) \end{cases} \quad (9)$$

$$\text{O2} : \begin{cases} I_{2\omega,p}^{\text{total}} = w_1 I_{2\omega,p}(\beta = 90^\circ) + w_2 I_{2\omega,p}(\beta = 180^\circ) + w_3 I_{2\omega,p}(\beta = 270^\circ) + (1 - w_1 - w_2 - w_3) I_{2\omega,p}(\beta = 0^\circ) \\ I_{2\omega,s}^{\text{total}} = w_1 I_{2\omega,s}(\beta = 90^\circ) + w_2 I_{2\omega,s}(\beta = 180^\circ) + w_3 I_{2\omega,s}(\beta = 270^\circ) + (1 - w_1 - w_2 - w_3) I_{2\omega,s}(\beta = 0^\circ) \end{cases} \quad (10)$$

Where w_1, w_2, w_3 , are the area fraction of three of the four domain variants in the probed area. The fits reveal these factors to be $\sim 1/4$ each as suggested by COBRA results.

Code availability. The computer codes that support the findings of this study are available from the corresponding author upon reasonable request.

Data availability

The data that support the findings of this study are available from the corresponding author upon reasonable request.

Received: 31 May 2018 Accepted: 12 November 2018

Published online: 06 December 2018

References

- Zubko, P., Gariglio, S., Gabay, M., Ghosez, P. & Triscone, J.-M. Interface physics in complex oxide heterostructures. *Annu. Rev. Condens. Matter Phys.* **2**, 141–165 (2011).
- Feature, N. Enter the oxides. *Nature* **459**, 28–30 (2009).
- Hwang, H. Y. et al. Emergent phenomena at oxide interfaces. *Nat. Mater.* **11**, 103–113 (2012).
- Chakhalian, J., Millis, A. J. & Rondinelli, J. Whither the oxide interface. *Nat. Mater.* **11**, 92–94 (2012).
- Mannhart, J. & Schlom, D. G. Oxide interfaces—an opportunity for electronics. *Science* **327**, 1607–1611 (2010).
- Hellman, F. et al. Interface-induced phenomena in magnetism. *Rev. Mod. Phys.* **89**, 1–79 (2017).
- Stengel, M., Vanderbilt, D. & Spaldin, N. A. Enhancement of ferroelectricity at metal-oxide interfaces. *Nat. Mater.* **8**, 392–397 (2009).
- Chakhalian, J. et al. Orbital reconstruction and covalent bonding at an oxide. *Interface Sci.* **318**, 1114–1117 (2007).
- Ohtomo, A. & Hwang, H. Y. A high-mobility electron gas at the LAO₃/STO₃ heterointerface. *Nature* **427**, 423–426 (2004).
- Reyren, N. et al. Superconducting interfaces between insulating oxides. *Science* **317**, 1196–1199 (2007).
- Xiao, D., Zhu, W., Ran, Y., Nagaosa, N. & Okamoto, S. Interface engineering of quantum Hall effects in digital transition metal oxide heterostructures. *Nat. Commun.* **2**, 596–598 (2011).
- Aetukuri, N. B. et al. Control of the metal–insulator transition in vanadium dioxide by modifying orbital occupancy. *Nat. Phys.* **9**, 661–666 (2013).
- Schlom, D. G. et al. Strain tuning of ferroelectric thin films. *Annu. Rev. Mater. Res.* **37**, 589–626 (2007).
- Zhang, L. et al. Continuously tuning epitaxial strains by thermal mismatch. *ACS Nano* **12**, 1306–1312 (2018).
- Mundy, J. A. et al. Atomically engineered ferroic layers yield a room-temperature magnetoelectric multiferroic. *Nature* **537**, 523–527 (2016).
- Yadav, A. K. et al. Observation of polar vortices in oxide superlattices. *Nature* **530**, 198–201 (2016).
- Boris, A. V. et al. Dimensionality control of electronic phase transitions in nickel-oxide superlattices. *Science* **332**, 937–940 (2011).
- Kan, D. et al. Tuning magnetic anisotropy by interfacially engineering the oxygen coordination environment in a transition metal oxide. *Nat. Mater.* **15**, 1–7 (2016).
- Wang, H. et al. Stabilization of highly polar BiFeO₃-like structure: a new interface design route for enhanced ferroelectricity in artificial perovskite superlattices. *Phys. Rev. X* **6**, 1–8 (2016).
- Kim, T. H. et al. Polar metals by geometric design. *Nature* **533**, 68–72 (2016).
- Yu, P. et al. Interface control of bulk ferroelectric polarization. *Proc. Natl Acad. Sci. USA* **109**, 9710–9715 (2012).
- Liao, Z. et al. Controlled lateral anisotropy in correlated manganese heterostructures by interface-engineered oxygen octahedral coupling. *Nat. Mater.* **15**, 425–431 (2016).
- Cao, Y. et al. Artificial two-dimensional polar metal at room temperature. *Nat. Commun.* **9**, 1547 (2018).
- Bousquet, E. et al. Improper ferroelectricity in perovskite oxide artificial superlattices. *Nature* **452**, 732–736 (2008).
- Oh, Y. S., Luo, X., Huang, F.-T., Wang, Y. & Cheong, S.-W. Experimental demonstration of hybrid improper ferroelectricity and the presence of abundant charged walls in (Ca,Sr)₃Ti₂O₇ crystals. *Nat. Mater.* **14**, 407–413 (2015).
- Rondinelli, J. M., May, S. J. & Freeland, J. W. Control of octahedral connectivity in perovskite oxide heterostructures: an emerging route to multifunctional materials discovery. *MRS Bull.* **37**, 261–270 (2012).
- Benedek, N. A., Mulder, A. T. & Fennie, C. J. Polar octahedral rotations: a path to new multifunctional materials. *J. Solid State Chem.* **195**, 11–20 (2012).
- Rondinelli, J. M. & Fennie, C. J. Octahedral rotation-induced ferroelectricity in cation ordered perovskites. *Adv. Mater.* **24**, 1961–1968 (2012).
- Gao, R. et al. Interfacial octahedral rotation mismatch control of the symmetry and properties of SrRuO₃. *ACS Appl. Mater. Interfaces* **8**, 14871–14878 (2016).
- Jaramillo, R., Ha, S. D., Silevitch, D. M. & Ramanathan, S. Origins of bad-metal conductivity and the insulator-metal transition in the rare-earth nickelates. *Nat. Phys.* **10**, 304–307 (2014).
- Yacoby, Y. et al. Direct determination of epitaxial interface structure in Gd₂O₃ passivation of GaAs. *Nat. Mater.* **1**, 99–101 (2002).
- Zhou, H., Pindak, R., Clarke, R., Steinberg, D. M. & Yacoby, Y. The limits of ultrahigh-resolution x-ray mapping: estimating uncertainties in thin-film and interface structures determined by phase retrieval methods. *J. Phys. D Appl. Phys.* **45**, 195302 (2012).
- Pauli, S. A., Leake, S. J., Björck, M. & Willmott, P. R. Atomic imaging and direct phase retrieval using anomalous surface X-ray diffraction. *J. Phys. Condens. Matter* **24**, 305002 (2012).
- Zhou, H. et al. Anomalous expansion of the copper-apical-oxygen distance in superconducting cuprate bilayers. *Proc. Natl Acad. Sci. USA* **107**, 8103–8107 (2010).
- Kumah, D. P., Shusterman, S., Paltiel, Y., Yacoby, Y. & Clarke, R. Atomic-scale mapping of quantum dots formed by droplet epitaxy. *Nat. Nanotechnol.* **4**, 835–838 (2009).
- Willmott, P. R. et al. Structural basis for the conducting interface between LaAlO₃ and SrTiO₃. *Phys. Rev. Lett.* **99**, 155502 (2007).
- Kumah, D. P. et al. Tuning the structure of nickelates to achieve two-dimensional electron conduction. *Adv. Mater.* **26**, 1935–1940 (2014).
- Wakabayashi, Y., Takeya, J. & Kimura, T. Sub-Å resolution electron density analysis of the surface of organic rubrene crystals. *Phys. Rev. Lett.* **104**, 066103 (2010).
- Morisaki, H. et al. Large surface relaxation in the organic semiconductor tetracene. *Nat. Commun.* **5**, 5400 (2014).
- Björck, M. et al. Atomic imaging of thin films with surface x-ray diffraction: introducing DCAF. *J. Phys. Condens. Matter* **20**, 445006 (2008).

41. Kumah, D. P., Yacoby, Y., Pauli, S. A., Willmott, P. R. & Clarke, R. La-doped BaTiO₃ heterostructures: compensating the polarization discontinuity. *APL Mater.* **1**, 062107 (2013).
42. Miao, J., Ishikawa, T., Robinson, I. K. & Murnane, M. M. Beyond crystallography: diffractive imaging using coherent X-ray light sources. *Science* **348**, 530–535 (2015).
43. Chen, C.-C. C. et al. Three-dimensional imaging of dislocations in a nanoparticle at atomic resolution. *Nature* **496**, 74–77 (2013).
44. Ludwig, W. et al. Three-dimensional imaging of crystal defects by ‘topotomography’. *J. Appl. Crystallogr.* **34**, 602–607 (2001).
45. Raines, K. S. et al. Three-dimensional structure determination from a single view. *Nature* **463**, 214–217 (2010).
46. Eklund, C.-J., Fennie, C. J. & Rabe, K. M. Strain-induced ferroelectricity in orthorhombic CaTiO₃ from first principles. *Phys. Rev. B* **79**, 220101 (2009).
47. Gu, Y., Rabe, K., Bousquet, E., Gopalan, V. & Chen, L.-Q. Phenomenological thermodynamic potential for CaTiO₃ single crystals. *Phys. Rev. B* **85**, 64117 (2012).
48. Haislmaier, R. C. et al. Unleashing strain induced ferroelectricity in complex oxide thin films via precise stoichiometry control. *Adv. Funct. Mater.* **26**, 7271–7279 (2016).
49. Biegalski, M. D. et al. Impact of symmetry on the ferroelectric properties of CaTiO₃ thin films. *Appl. Phys. Lett.* **106**, 162904 (2015).
50. Glazer, A. M. Simple ways of determining perovskite structures. *Acta Crystallogr. Sect. A* **31**, 756–762 (1975).
51. Glazer, A. The classification of tilted octahedra in perovskites. *Acta Crystallogr. Sect. B* **28**, 3384–3392 (1972).
52. Fister, T. T. et al. Octahedral rotations in strained LaAlO₃/SrTiO₃ (001) heterostructures. *APL Mater.* **2**, 021102 (2014).
53. Benedek, N. A. & Fennie, C. J. Why are there so few perovskite ferroelectrics? *J. Phys. Chem. C* **117**, 13339–13349 (2013).
54. Bonabeau, E. et al. High-energy surface X-ray diffraction for fast surface structure determination. *Science* **343**, 758–762 (2014).
55. Yacoby, Y. et al. Direct determination of epitaxial film and interface structure: Gd₂O₃ on GaAs (1 0 0). *Phys. B Condens. Matter* **336**, 39–45 (2003).
56. Björck, M. & Andersson, G. GenX: an extensible X-ray reflectivity refinement program utilizing differential evolution. *J. Appl. Crystallogr.* **40**, 1174–1178 (2007).
57. Blöchl, P. E. Projector augmented-wave method. *Phys. Rev. B* **50**, 17953–17979 (1994).
58. Kresse, G. & Furthmüller, J. Efficient iterative schemes for ab initio total-energy calculations using a plane-wave basis set. *Phys. Rev. B* **54**, 11169–11186 (1996).
59. Perdew, J. P., Burke, K. & Ernzerhof, M. Generalized gradient approximation made simple. *Phys. Rev. Lett.* **77**, 3865–3868 (1996).
60. Lei, S. et al. Observation of quasi-two-dimensional polar domains and ferroelastic switching in a metal, Ca₃Ru₂O₇. *Nano Lett.* **18**, 3088–3095 (2018).
61. Guo, J. W. et al. Strain-induced ferroelectricity and spin-lattice coupling in SrMnO₃ thin films. *Phys. Rev. B* **97**, 235135 (2018).

Acknowledgements

This work was supported by National Science Foundation (NSF) MRSEC Center for Nanoscale Science under award no. DMR-1420620. This research used resources of the Advanced Photon Source, a U.S. Department of Energy (DOE) Office of Science User

Facility operated by Argonne National Laboratory under Contract No. DE-AC02-06CH11357. The DFT study is conducted as part of The Pennsylvania State University (PSU) 2D Crystal Consortium – Materials Innovation Platform (2DCC-MIP) under NSF award No. DMR-1539916. Support was also received from the PSU’s Institute for CyberScience (ICS) through a Graduate Research Assistantship. Computations for this research were performed on the PSU’s Institute for CyberScience Advanced CyberInfrastructure (ICS-ACI). This content is solely the responsibility of the authors and does not necessarily represent the views of the ICS. This work made use of the Cornell Center for Materials Research (CCMR) Shared Facilities, which are supported through the NSF MRSEC program (DMR-1719875). Substrate preparation was performed in part at the Cornell NanoScale Science & Technology Facility, a member of the National Nanotechnology Coordinated Infrastructure (NNCI), which is supported by the NSF ECCS-1542081. We thank Zhan Zhang for the help with synchrotron XRD at APS-33ID and Haiying Wang from the Materials Characterization Laboratory at Penn State for the help with STEM sample preparation.

Author contributions

Y.Y. and H.Z. performed the synchrotron CTR measurements and COBRA analysis. Y.L. and S.B.S. formulated the model and performed DFT calculations. K.W., Y.Y., and G.S. carried out scanning transmission electron microscopy studies. C.M.B. synthesized the samples with advice from D.G.S. Y.Y. and V.G. performed optical SHG measurements. Y. Y., D.G.S., S.B.S., H.Z., and V.G. prepared the manuscript. All authors discussed the results.

Additional information

Supplementary Information accompanies this paper at <https://doi.org/10.1038/s41467-018-07665-1>.

Competing interests: The authors declare no competing interests.

Reprints and permission information is available online at <http://npg.nature.com/reprintsandpermissions/>

Publisher’s note: Springer Nature remains neutral with regard to jurisdictional claims in published maps and institutional affiliations.



Open Access This article is licensed under a Creative Commons Attribution 4.0 International License, which permits use, sharing, adaptation, distribution and reproduction in any medium or format, as long as you give appropriate credit to the original author(s) and the source, provide a link to the Creative Commons license, and indicate if changes were made. The images or other third party material in this article are included in the article’s Creative Commons license, unless indicated otherwise in a credit line to the material. If material is not included in the article’s Creative Commons license and your intended use is not permitted by statutory regulation or exceeds the permitted use, you will need to obtain permission directly from the copyright holder. To view a copy of this license, visit <http://creativecommons.org/licenses/by/4.0/>.

© The Author(s) 2018

- 1 Supplementary Material
- 2 **Three-dimensional Atomic Scale Electron Density Reconstruction of**
- 3 **Octahedral Tilt Epitaxy in Functional Perovskites**
- 4 Yuan, *et al.*

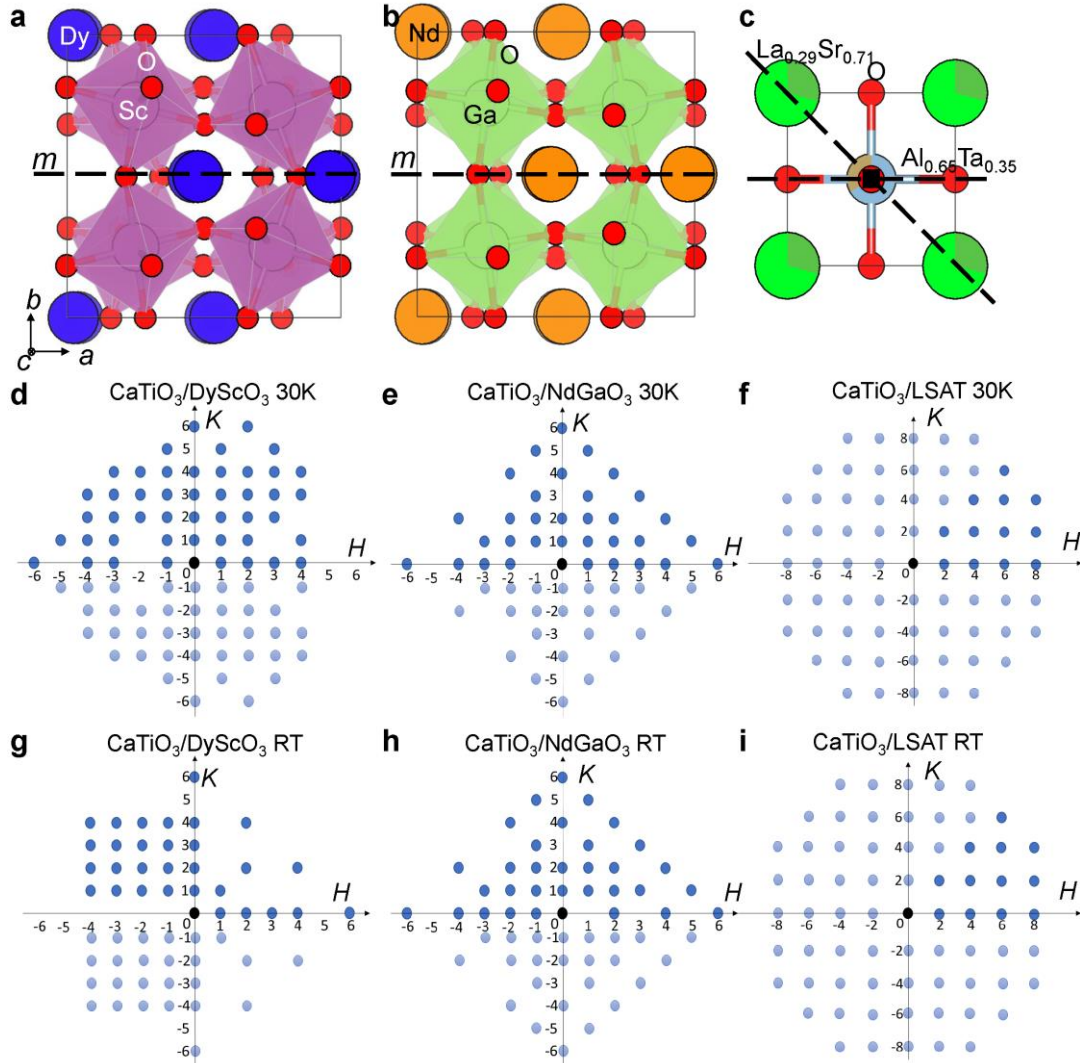
5 **Supplementary Table 1 | Comparison between coherent Bragg rods analysis and other**
6 **imaging techniques.**

	CDI	TEM/STEM	COBRA
Probe beam	X-ray/Electron beam	Electron beam	X-ray
Beam coherency requirement	Fully coherent (>scale of sample)	No requirement	Axial coherence >> film thickness
Sample type	Objects with clear boundaries, e.g. nanoparticles	Specially prepared ultrathin sample	Epitaxial thin film systems
Sample size	Hundreds nm to several microns	Sample thickness <100 nm	Film thickness <20 nm
Sample environment	Mostly non-destructive; in-situ/operando feasible	Destructive; in-situ/operando feasible but challenging	Non-destructive; in-situ/operando routine
Beam stability	Very high stability (long exposure time)	Very high stability	Normal (strong diffraction, shorter exposure time)
Coverage of reciprocal space	Low	Not applicable	High
Best resolution achieved	~5.5 nm in 3D	~40 pm in 2D	~40 pm in 3D
Data processing method	Phase retrieval algorithm	Image processing	Phase retrieval algorithm
Data acquisition time	~ 2 hours	~ 2 min per image	~ 6 hours

7 **Supplementary Note 1: Symmetry based crystal truncation rods measurements**

8 In order to reconstruct electron densities (EDs) in real space using Fourier phase retrieval
9 algorithm, coherent Bragg rods analysis (COBRA) method requires the measurement of crystal
10 truncation rods (CTRs) in the whole reciprocal space. This usually requires a large group of
11 CTRs to be collected. In practice, giving the fact that symmetry equivalent CTRs will be
12 identical to each other, therefore, only symmetry inequivalent CTRs are measured and used to
13 recover the diffraction phase information in the whole reciprocal space. Furthermore, the
14 symmetry of the epitaxial systems is usually dictated by the substrates. In this work, substrates
15 $\text{NdGaO}_3(110)_{\text{or}}$ (or: orthorhombic) and $\text{DyScO}_3(110)_{\text{or}}$ of bulk space group of *Pnma*, with
16 termination at their $(110)_{\text{or}}$ planes, will only retain one of their mirror symmetry for the epitaxial
17 systems, as shown in Supplementary Figures 1a and b. As for LSAT substrate, *4mm* symmetry is
18 retained for $(001)_{\text{pc}}$ (pc: pseudocubic) termination (Supplementary Figure 1c). The presence of
19 above symmetries was also confirmed by experiments discussed in Supplementary Note 2.
20 Accordingly, the CTRs measured experimentally are illustrated in Supplementary Figures 1d-i
21 using dark blue dots in reciprocal lattice, while the CTRs recovered by symmetry are indicated
22 using light blue dots. All the (H, K) values are under $2 \times 2 \times 2$ pseudocubic notation.

23



24

25 **Supplementary Figure 1 | Symmetry of epitaxial systems and experimentally measured**
 26 **crystal truncation rods.** Symmetry analysis of terminated substrates show that **a** $\text{DyScO}_3(110)_{\text{or}}$
 27 and **b** $\text{NdGaO}_3(110)_{\text{or}}$ has only one mirror symmetry. **c**, $\text{LSAT}(001)_{\text{pc}}$ has $4mm$ point group
 28 symmetry. **d-i**, Experimentally measured (H, K) crystal truncation rods (CTRs) for three
 29 different epitaxial systems under 30K and room temperature (RT) are marked by dark blue dots.
 30 The symmetry equivalent CTRs in each system are indicated by light blue dots. Experimentally
 31 measured $(0, 0)$ specular CTRs are shown using black dots. All the (H, K) values are under
 32 $2 \times 2 \times 2$ pseudocubic notation.

33 **Supplementary Note 2: Domain states of epitaxial CaTiO₃ on NdGaO₃, DyScO₃, and LSAT**

34 The domain states of the epitaxial CaTiO₃ thin film are analyzed from three perspectives:
35 substrates symmetry and CTRs, optical second harmonic generation (SHG) polarimetry study,
36 and real space structures determined by COBRA and scanning transmission electron microscopy
37 (STEM).

38

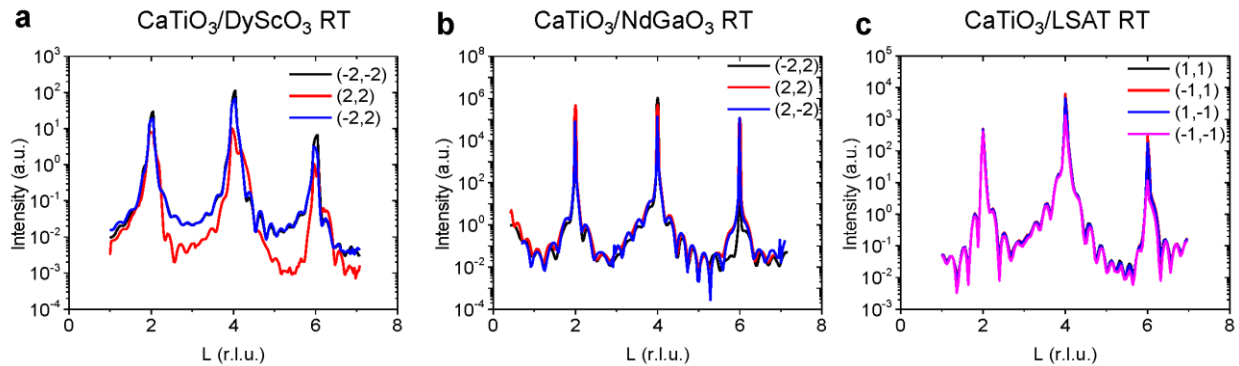
39 From the substrate symmetry perspective, both NdGaO₃ and DyScO₃ have the same bulk space
40 group of *Pnma* as CaTiO₃. Epitaxially grown CaTiO₃ thin films are expected to follow the exact
41 same orientation as substrate to achieve coherent structure across the interface and minimize
42 their interfacial energy. This can be verified by the symmetry of CTRs in these two systems,
43 where only a mirror plane perpendicular to *b* axis exists, giving CTRs equivalence of $(H, K) = (H,$
44 $-K)$ as shown in Supplementary Figure 2. Using $2 \times 2 \times 2$ pseudocubic notation, for
45 CaTiO₃/DyScO₃ (Supplementary Figure 2a), $(-2,2)$ rod is equivalent to $(-2,-2)$ rod and
46 inequivalent to $(2,2)$ rod. Similarly, in Supplementary Figure 2b for CaTiO₃/NdGaO₃, $(2,2)$ rod is
47 equivalent to $(2,-2)$ rod and inequivalent to $(-2,2)$ rod. As for CaTiO₃/LSAT, since substrate
48 LSAT has *4mm* symmetry considering the surface termination, orthorhombic CaTiO₃ is expected
49 to form 4 symmetry equivalent domains with in-plane rotation 90° to each other, with similar
50 domain fractions. This will give rise to a macroscopic *4mm* symmetry in CTR measurement,
51 where $(2,2)$, $(-2,2)$, $(2,-2)$, and $(-2,-2)$ rods are equivalent to each other, as shown in
52 Supplementary Figure 2c.

53 Symmetry of the three epitaxial systems is also verified by the SHG polarimetry study as shown
54 in Fig. 5c and Supplementary Figure 10. A mirror symmetry is observed for CaTiO₃/DyScO₃ and

55 CaTiO₃/NdGaO₃, with single domain theoretical fitting to their SHG polarimetry data. For
 56 CaTiO₃/LSAT, a *4mm* symmetry is observed and polarimetry data is fitted by four equivalent
 57 domains with similar domain fractions.

58 From COBRA reconstructed EDs (Figs. 2a, b) for CaTiO₃/DyScO₃ and CaTiO₃/NdGaO₃, a
 59 coherent oxygen octahedra tilt pattern is observed from substrates to epitaxial thin films,
 60 indicating a single domain state of CaTiO₃ on these two substrates. This can also be verified by
 61 the STEM images shown in Figs. 4a, b, and Supplementary Figure 8. For CaTiO₃/LSAT, the
 62 successful reconstruction of ED (Fig. 2c) confirms the *4mm* symmetry, which originates from the
 63 multidomain nature of the system.

64



65

66 **Supplementary Figure 2 | Crystal truncation rods equivalence for the three systems.** The
 67 symmetry of each system can be identified by the equivalence of crystal truncation rods at room
 68 temperature (RT). **a**, CaTiO₃/DyScO₃ shows (-2,2) rod is equivalent to (-2,-2) rod and
 69 inequivalent to (2,2) rod. **b**, CaTiO₃/NdGaO₃ shows (2,2) rod is equivalent to (2,-2) rod and
 70 inequivalent to (-2,2) rod. **c**, CaTiO₃/LSAT shows (2,2), (-2,2), (2,-2), and (-2,-2) rods are
 71 equivalent.

72 **Supplementary Note 3: Folded structure and tilt pattern for CaTiO₃ on LSAT**

73 In the cases where thin film and substrate symmetries are different, the epitaxial thin film may
74 form different domains. However, only the CTRs defined by the substrate reciprocal lattice have
75 strong enough diffraction intensities and are measured during experiments. In this case, the
76 reconstructed thin film ED contains thin film structural information that is folded into substrate
77 defined in-plane unit cell. This folding process of CaTiO₃ on LSAT is illustrated in
78 Supplementary Figure 3, where four equivalent domains of CaTiO₃ are spatially translated by
79 LSAT lattice vectors into one folded structure.

80 The mathematical representation of this folding process is described as follows. The
81 multidomain ED of thin film ρ^{film} can be written as:

$$82 \quad \rho^{\text{film}}(\mathbf{r}) = \sum_{i,j} \rho_{i,j}^{\text{film,uc}}(\mathbf{r} - i\mathbf{R}_1 - j\mathbf{R}_2) \quad (1)$$

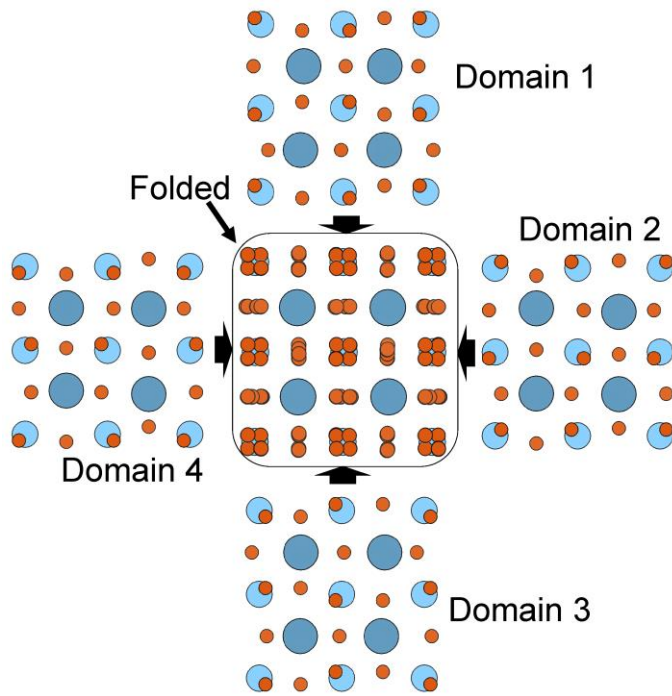
83 Where $\rho_{i,j}^{\text{film,uc}}$ is the electron density of the unit cell origins at $i\mathbf{R}_1 + j\mathbf{R}_2$, \mathbf{R}_1 , \mathbf{R}_2 are
84 translational vectors defined by the substrate lattice. The diffraction contributed by thin film can
85 be rewritten as:

$$86 \quad I^{\text{film}}(\mathbf{q}) \sim \sum_{H,K} |F_{q_1,q_2,q_3}(\overline{\rho_{i,j}^{\text{film,uc}}}) \delta(q_1 - HQ_1) \delta(q_2 - KQ_2)| \quad (2)$$

87 Where F_{q_1,q_2,q_3} is the Fourier transformation (FT) at reciprocal position (q_1, q_2, q_3) , Q_1 , Q_2 are in-
88 plane reciprocal lattice vectors of substrate, H , K are integers, $\overline{\rho_{i,j}^{\text{film,uc}}}$ is the average ED over i, j .
89 And δ function states the fact that only reciprocal positions along the crystal truncation rods have
90 significant diffraction intensities. Above equations suggest that, the folded ED is the average of

91 EDs in all unit cells, which are defined by the substrate translational vectors \mathbf{R}_1 and \mathbf{R}_2 , as shown
92 in Supplementary Figure 3.

93



94

95 **Supplementary Figure 3 | Folded structure of CaTiO₃ on LSAT.** Four symmetry equivalent
96 domains of CaTiO₃ are shown in the figure. The center structure is obtained by spatially
97 translating four domains into single unit cell defined by LSAT in-plane lattice vectors. The Ca,
98 Ti, and O atoms are indicated by dark blue, light blue, and red dots, respectively.

99

100 To determine the tilt pattern of CaTiO₃ on LSAT, we performed half order peak measurement.
101 According to our measurement, the LSAT substrate has cubic lattice parameters, but it contains
102 small double perovskite structural domains, which give rise to very broad and strong substrate
103 peaks at half order positions ($H, K, L = \text{half integers under pseudocubic notation}$), overwhelming

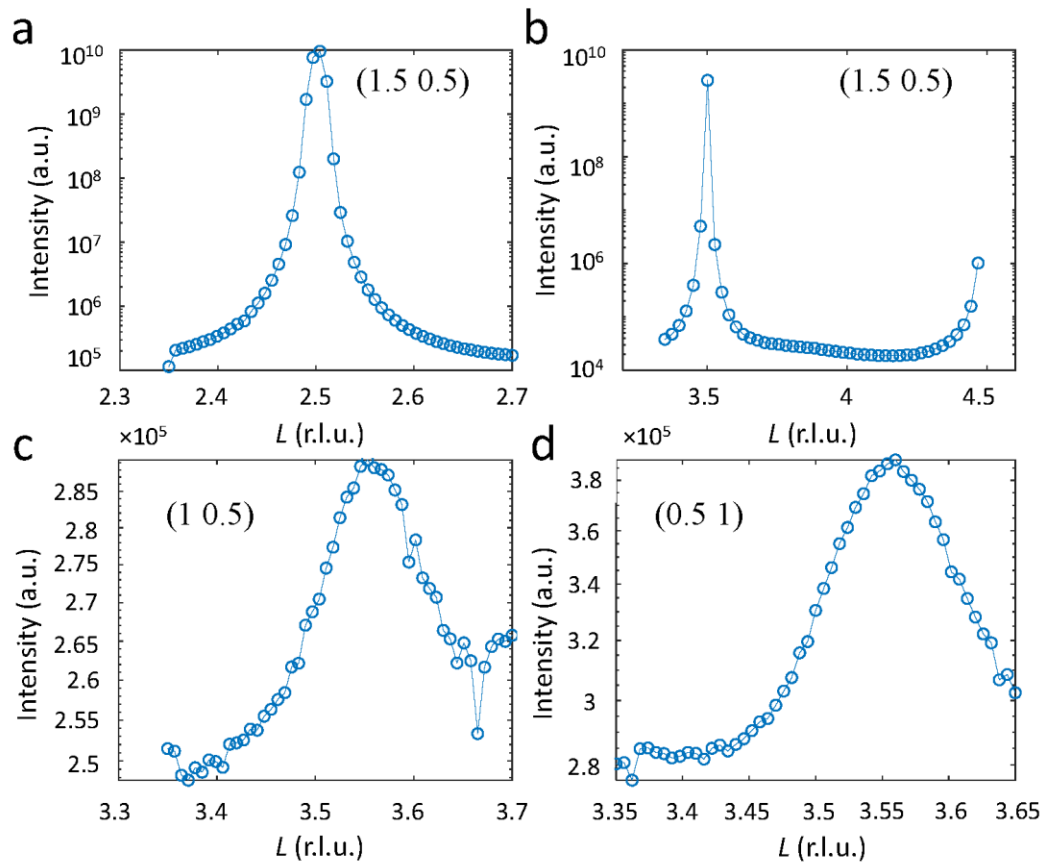
104 the weak CTO film peaks associated with all out-of-phase tilts, as seen in Supplementary Figure
105 4a. Thus, direct determination of out-of-phase tilts is not possible.

106 However, half order peaks associated with in-phase tilts at (odd/2, even/2, odd/2) or (even/2,
107 odd/2, odd/2) are observed as shown in Supplementary Figures 4c and d, suggesting in-phase
108 tilts about a - and b -axes. Since CTO film on LSAT has four equivalent in-plane directions and
109 we do not observe a double peak feature, different from the results in ref.¹, these peaks should be
110 explained by multidomain states of a single in-phase tilt along a - or b -axis (not both).

111 We also confirm that the absence of (1.5 0.5 4) peak (Supplementary Figure 4b), suggesting an
112 out-of-phase or no tilt along c -axis. Hence, we conclude from the half order peak results that the
113 CTO on LSAT only has one in-phase tilt along one of the in-plane directions, and could have
114 out-of-phase tilts or no tilts along the other two axes.

115 However, COBRA results reveal a finite tilt along the c -axis, ruling out the possibility of c^0 .
116 Thus, $a^+b^{-0}c^-$ or $a^{-0}b^+c^-$ tilt pattern is expected. Moreover, our density functional theory (DFT)
117 study suggests a tilt pattern of $a^-b^+c^-$ in CTO on LSAT, and the most stable tilt pattern of CTO
118 under a similar strain state ($\sim 1\%$) on NGO substrate is $a^-b^+c^-$. Hence, we conclude that the CTO
119 on LSAT should adopt an $a^-b^+c^-/a^+b^-c^-$ mixed tilt pattern.

120



121

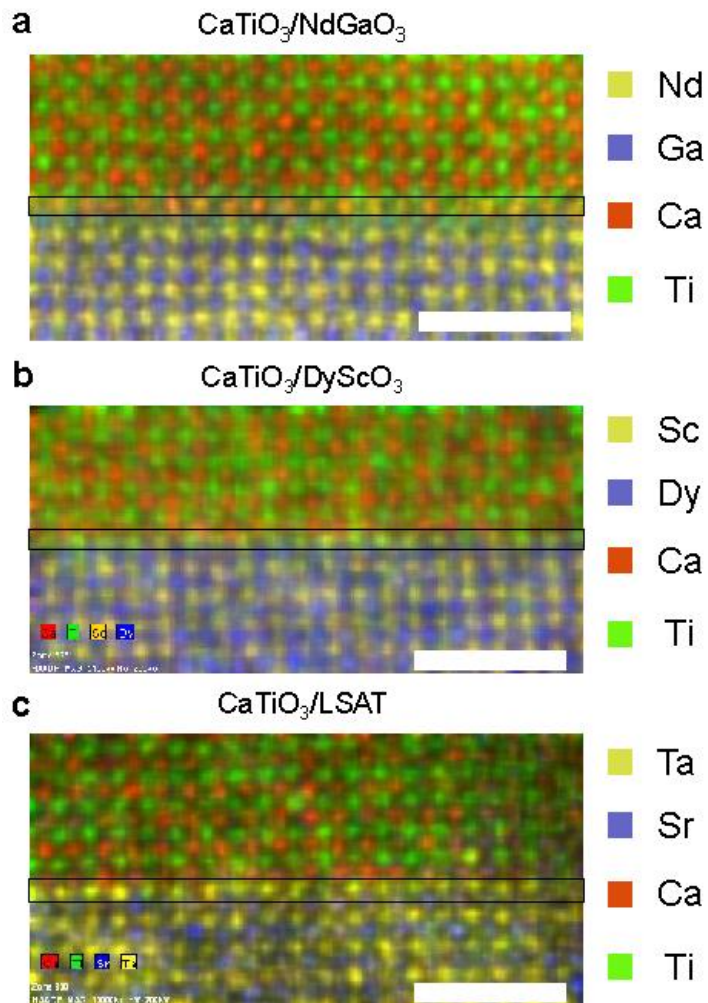
122 **Supplementary Figure 4 | Half order diffraction peaks of CaTiO₃ film on LSAT. a** Strong

123 $(1.5 \ 0.5 \ 2.5)$ peak from LSAT overwhelm the possible out-of-phase tilt peaks from CTO thin

124 film. **b** The absence of $(1.5 \ 0.5 \ 4)$ peak indicates a c^- or c^0 tilt about c -axis. **c-d** The single peak at

125 $(1 \ 0.5 \ 3.5)$ and $(0.5 \ 1 \ 3.5)$ position suggests the CTO on LSAT has only one in-phase tilt along

126 one of the in-plane axes.



127

128 **Supplementary Figure 5 | Energy dispersion spectrum mapping on the three systems.**

129 Energy dispersion spectrum (EDS) mapping on the three systems reveal termination of **a** NdO
 130 plane for $\text{CaTiO}_3/\text{NdGaO}_3$ **b** ScO_2 plane for $\text{CaTiO}_3/\text{DyScO}_3$, and **c** $\text{Al}_{0.65}\text{Ta}_{0.35}\text{O}_2$ plane for
 131 $\text{CaTiO}_3/\text{LSAT}$. The solid black boxes mark the surface layer of substrates. The scale bars are 2
 132 nm.

133 **Supplementary Table 2 | Octahedral tilt angles for different substrates and CaTiO₃ thin**
 134 **films averaged over the entire film. (RT: room temperature)**

		$\alpha/^\circ$	$\beta/^\circ$	$\gamma/^\circ$	Tilt mismatch $ \Delta\alpha + \Delta\beta /^\circ$
Free bulk, Density functional theory (DFT)	CaTiO ₃ (CTO)	9.09	9.18	9.09	-
	NdGaO ₃ (NGO)	10.31	9.8	10.32	-
	DyScO ₃ (DSO)	15	13	15	-
	LSAT	0	0	0	-
Strained CaTiO ₃ bulk, DFT	1.1% (NGO)	9.37	9.53	8.15	1.21
	3.3% (DSO)	8.32	11.18	7.43	8.5
	1.2% (LSAT)	9.27	9.61	8.07	18.88
Epitaxial CaTiO ₃ , DFT	CTO/NGO	9.86	9.98	8.26	0.63
	CTO/DSO	11.04	10.63	7.76	6.33
	CTO/LSAT	3.92	4.66	8.1	8.58
Epitaxial CaTiO ₃ , COBRA 30K	CTO/NGO	9.91±0.35	9.53±0.35	7.71±0.35	0.67±0.49
	CTO/DSO	12.18±1.06	12.08±0.71	8.15±1.06	3.74±1.28
	CTO/LSAT	6.34±0.71	6.34±0.71	8.15±1.06	12.68±1.00
Epitaxial CaTiO ₃ , COBRA RT	CTO/NGO	12.00±1.06	10.50±0.35	7.90±1.06	2.39±1.12
	CTO/DSO	11.00±1.06	10.00±0.71	8.10±0.71	7.00±1.28
	CTO/LSAT	5.50±0.71	5.50±0.71	8.10±1.06	11.00±1.00

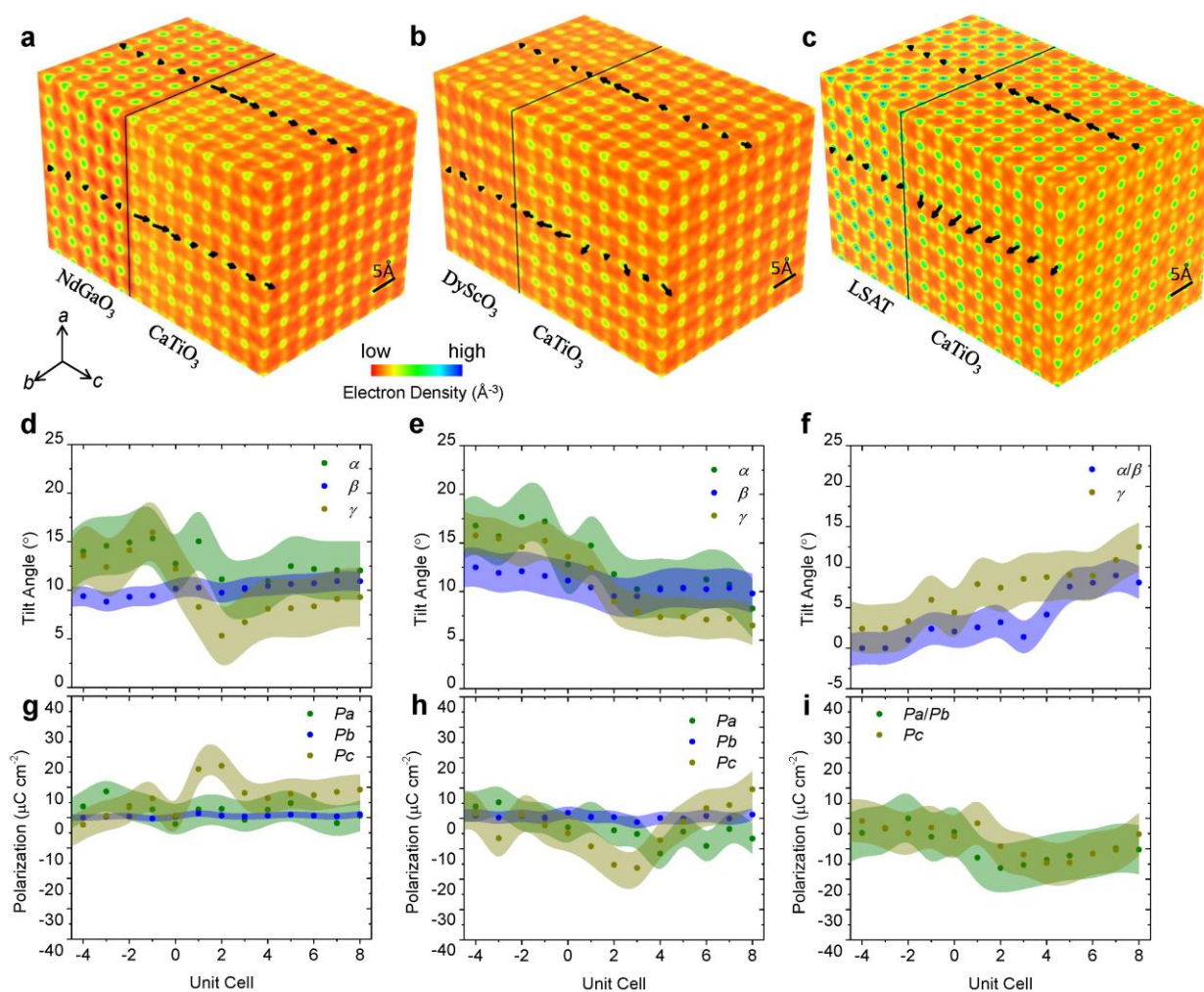
136 **Supplementary Note 4: Room temperature EDs by COBRA and polarization by STEM**

137 Room temperature EDs reconstructed by COBRA for CaTiO₃/NdGaO₃, CaTiO₃/DyScO₃,
138 CaTiO₃/LSAT are respectively plotted in Supplementary Figures 6a-c. Detailed octahedral tilt
139 angles for above three systems are shown in Supplementary Figures 6d, e and f. Due to the
140 interfacial tilt epitaxy effect, α and β values show more gradual change across the interface
141 compared to γ angles. Polarization components, P_a , P_b , P_c , in Supplementary Figures 6g and h
142 reveal a small out-of-plane polarization, P_c (yellow dots), near the interfaces, due to the valence
143 mismatch effect. The in-plane polarization components are zero for CaTiO₃/NdGaO₃, indicating
144 its paraelectric state at room temperature. CaTiO₃/DyScO₃ has a small but non-zero polarization
145 along a -axis (green dots in Supplementary Figure 6h), which indicates the system is close to its
146 Curie temperature and consistent with SHG results shown in Fig. 5b. The valence mismatch
147 effect is less clear in CaTiO₃/LSAT (yellow dots in Supplementary Figure 6i) due to the smallest
148 valence mismatch value (-0.3) among all three systems as discussed in the main text. However, a
149 clear in-plane polarization (green dots in Supplementary Figure 6i) with similar magnitude to 30
150 K results (Fig. 2f), reveals the CaTiO₃ on LSAT has the most stable ferroelectric state among all
151 three systems. The Curie temperature of this system is much higher than room temperature (>900
152 K), as revealed by SHG measurement in Fig. 5b.

153 The STEM measurement was performed at room temperature to probe the polarization in these
154 films. At room temperature, only the CTO film on LSAT displays significant polarization, which
155 is demonstrated by the COBRA results in Supplementary Figure 6 and temperature dependent
156 SHG results in Fig. 5b. However, we found that the polarizations extracted from STEM at room
157 temperature were quite noisy. As shown in Supplementary Figure 7, the error bars of the
158 polarization extracted from STEM on CTO/LSAT are quite significant when compared to the

159 mean values (solid lines). However, these mean values from STEM agree well with room
 160 temperature COBRA results (dots), suggesting non-zero polarizations in CTO along in-plane and
 161 out-of-plane directions. The fact that the COBRA error bar is smaller than that of STEM is
 162 probably due to the fact that X-ray diffraction employed in COBRA is macroscale in nature and
 163 the averaged structure information is being extracted over a large sample area.

164



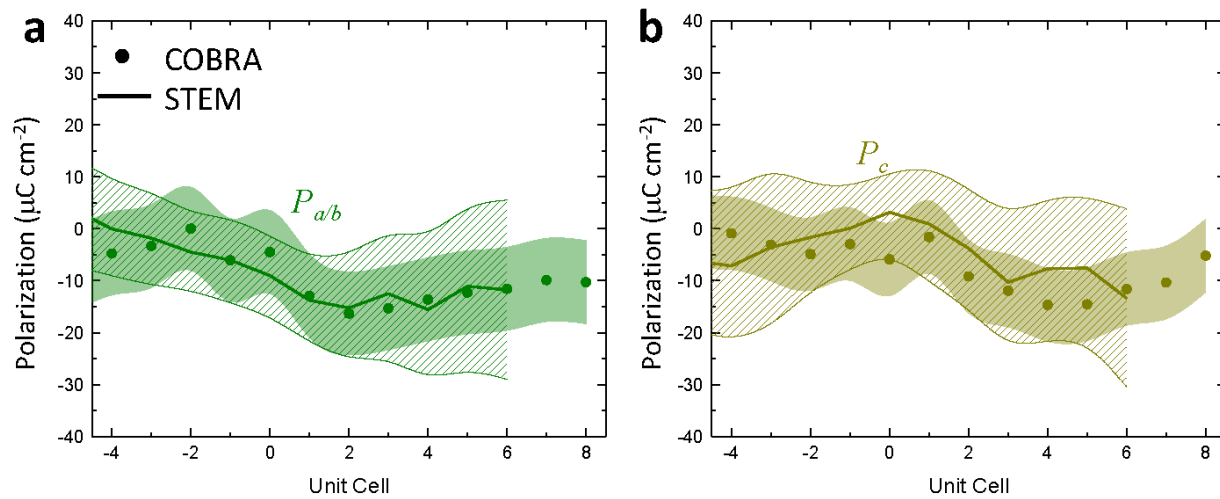
165

166 **Supplementary Figure 6 | Three-dimensional electron densities reconstructed by coherent Bragg**

167 **rods analysis at room temperature.** Three-dimensional (3D) electron densities (EDs) for a

168 $\text{CaTiO}_3/\text{NdGaO}_3$ **b** $\text{CaTiO}_3/\text{DyScO}_3$ **c** $\text{CaTiO}_3/\text{LSAT}$ at room temperature. One of the four equivalent
 169 CaTiO_3 domains on LSAT are plotted for convenience of comparison. In **d**, **e**, and **f**, quantified octahedral
 170 tilt angles, α (green), β (blue), γ (yellow), are shown, respectively. **g**, **h**, **i**, Polarization components, P_a
 171 (green), P_b (blue), P_c (yellow) extracted from COBRA (dots) are compared. The experimental errors are
 172 estimated by comparing substrates values to their reference bulk values and are indicated by the shaded
 173 area around the COBRA data dots.

174



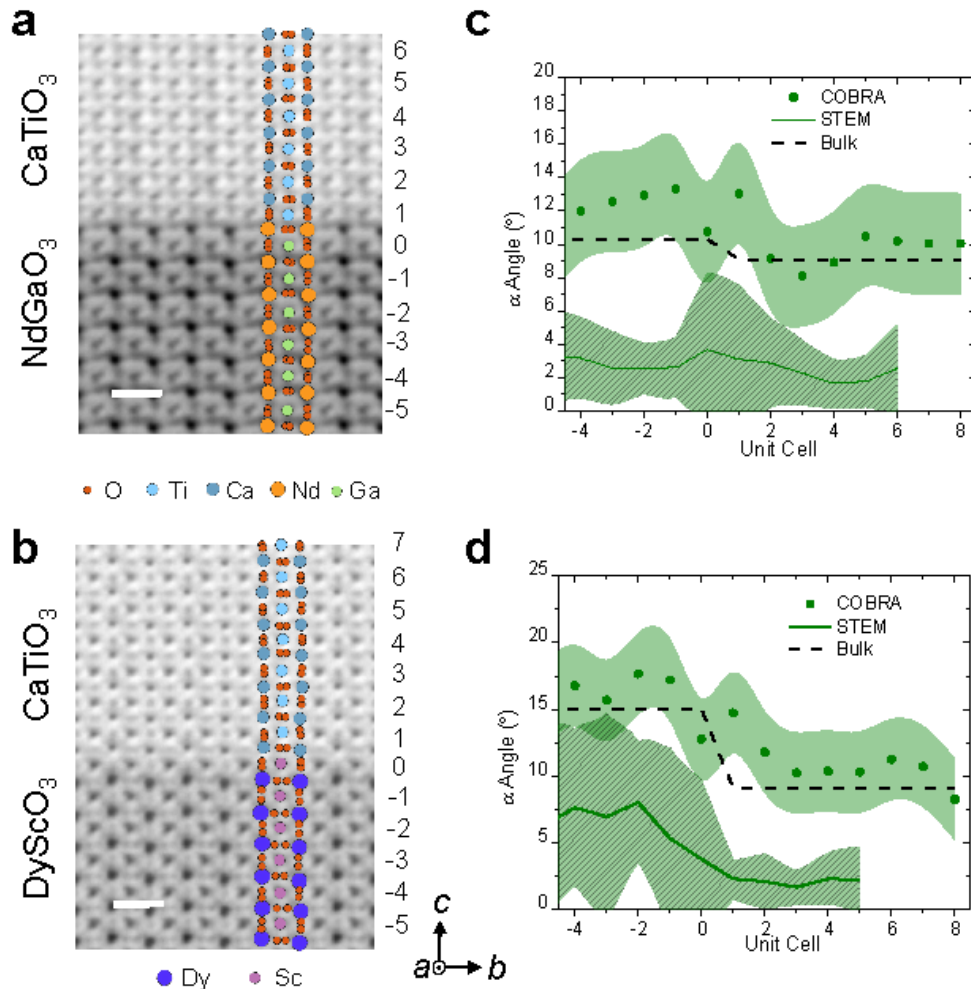
175

176 **Supplementary Figure 7 | Room temperature polarization in $\text{CaTiO}_3/\text{LSAT}$.** **a** In-plane and
 177 **b** out-of-plane polarization in $\text{CaTiO}_3/\text{LSAT}$ at room temperature probed by scanning
 178 transmission electron microscopy (STEM) (solid lines) and coherent Bragg rods analysis
 179 (COBRA) (dots). The STEM error bars are taken to be the standard deviations over around 20
 180 unit cells along the a/b -direction and are shown by the line shaded areas. The COBRA errors are
 181 estimated by comparing the substrate results to its bulk reference values, as shown by the color
 182 shaded areas.

183 **Supplementary Note 5: [100] zone axis STEM images on CaTiO₃ on NdGaO₃ and DyScO₃**

184 CaTiO₃, NdGaO₃ and DyScO₃ have out-of-phase tilts along [100] zone axis (α using Glazer
185 notation). STEM images along [100] zone axis reveal two oxygen columns close to each other on
186 oxygen sites, as illustrated by the left panel in Fig. 1a. The two oxygen columns in each pair are
187 too close to each other that they show up as one broadened oxygen peak in STEM projected
188 images, as shown in Supplementary Figure 8. By fitting the broadening of the oxygen peaks, the
189 α angles can be extracted from these images and are plotted in green lines in Supplementary
190 Figures 8c and d for CaTiO₃/NdGaO₃ and CaTiO₃/DyScO₃ respectively. However, the substrates
191 values are much smaller than expected values of $\sim 10.3^\circ$ for NdGaO₃ and $\sim 15^\circ$ for DyScO₃. In
192 contrast, room temperature COBRA reconstructed EDs on these two systems provides a 3D view
193 of the oxygen octahedral tilts and overcomes the overlapping problem of the oxygen peaks. The
194 α angles from COBRA method are plotted using green dots, which are much closer to the
195 expected values for bulk substrates.

196



197

198 **Supplementary Figure 8 | Room temperature STEM along [100] zone axis and α tilt angles.**

199 [100] zone axis scanning transmission electron microscopy (STEM) images for **a**

200 CaTiO₃/NdGaO₃ and **b** CaTiO₃/DyScO₃ at room temperature reveal broadened oxygen peaks

201 due to the out-of-phase tilt along *a*-axis. Different unit cells are numbered on the right side of the

202 images. The scale bars are 5 Å. In **c** and **d**, α angles obtained by fitting the broadening of the

203 oxygen peaks in STEM images (green lines) show smaller values than the expected bulk values

204 (dashed lines). Room temperature coherent Bragg rods analysis (COBRA) (green dots) gives

205 values much closer to that of bulk substrates, which are ~10.3° for NdGaO₃ and ~15.0° for

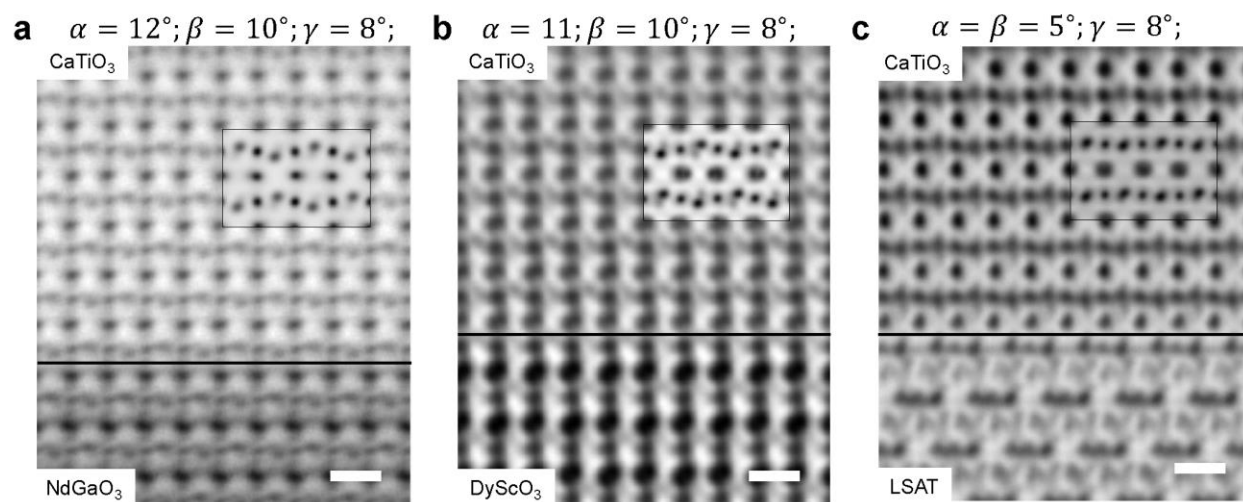
206 DyScO₃. The STEM error bars are taken to be the standard deviations over around 20 unit cells

207 along the b -direction and are shown by the line shaded areas. The COBRA errors are estimated
208 by comparing the substrate results to its bulk reference values, as shown by the green shaded
209 areas.

210 **Supplementary Note 6: [110] zone axis STEM images on CaTiO₃ on NdGaO₃, DyScO₃ and**
211 **LSAT**

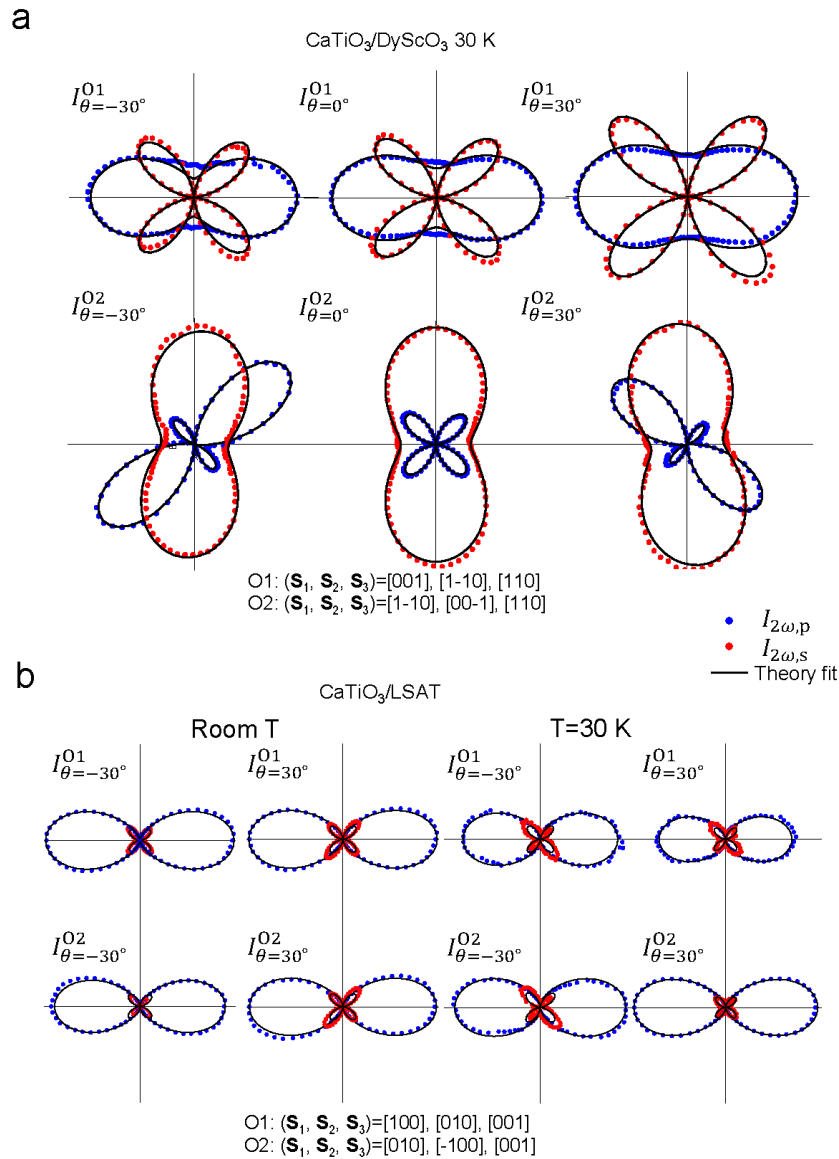
212 Oxygen tilts can be probed by comparing the [110] zone axis STEM images with theoretical
213 simulations, as proposed by Q.He, *et al.*² Samples of CaTiO₃/NdGaO₃, CaTiO₃/DyScO₃ and
214 CaTiO₃/LSAT were thinning down to ~50 nm for STEM imaging. The detector collecting angles
215 for the three systems were 9-50 mrad (CaTiO₃/NdGaO₃), 0–15 mrad (CaTiO₃/DyScO₃) and 1-15
216 mrad (CaTiO₃/LSAT). The experimental STEM images are shown in Supplementary Figure 9.
217 Theoretical simulations (inserts) for CaTiO₃ used $a^-b^+c^-$ tilt pattern with tilt angles resolved by
218 COBRA method, as listed in Supplementary Table 2. The experimental STEM images and
219 simulations matches qualitatively well with each other, supporting the results of COBRA
220 measurement. However, quantitative STEM analysis on the tilt angles requires resolving the
221 subtle shapes of oxygen projection along [110] zone axis, which is still quite challenging.

222



224 **Supplementary Figure 9 | Room temperature STEM along [110] zone axis.** [110] zone axis
225 scanning transmission electron microscopy (STEM) images on **a** CaTiO₃/NdGaO₃, **b**

226 CaTiO₃/DyScO₃ and **c** CaTiO₃/LSAT at room temperature reveal broadened oxygen peaks due to
227 the tilt of the oxygen octahedra. The theoretical simulated images (inserts) for CaTiO₃ with a^-
228 b^+c^- tilt pattern and COBRA resolved angles, which are specified above their images, are
229 compared to the experimental images. The simulation and experiment qualitatively match with
230 each other. The scale bars are 5 Å.



231

232 **Supplementary Figure 10 | SHG polarimetry of CaTiO₃/DyScO₃ and CaTiO₃/LSAT.**

233 Polarimetry data of p- (blue dots) and s- (red dots) polarized signal were measured under three

234 incident angles $\theta=-30^\circ$, 0° and 30° and two sample orientations, O1 and O2, for **a**

235 CaTiO₃/DyScO₃ at 30 K and **b** CaTiO₃/LSAT at room temperature and 30 K. Theoretical fitting

236 (black lines) reveals a single domain monoclinic *m* symmetry for CaTiO₃/DyScO₃ at 30 K and

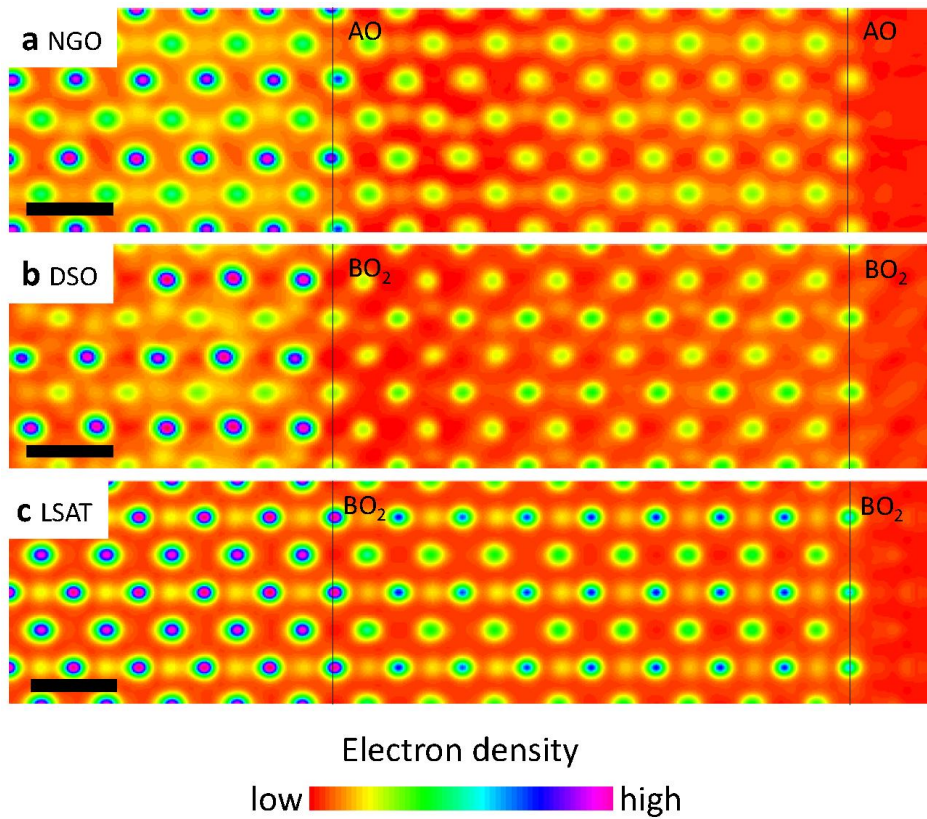
237 four equivalent *m* domains for CaTiO₃/LSAT.

238 **Supplementary Note 7: Termination of the CaTiO₃ films**

239 The CaTiO₃ termination of the three systems can be seen clearly in the (110) pseudocubic planes
240 as shown in Supplementary Figure 11, where alternating AO and BO₂ layers are directly visible.
241 We can see that the CTO terminations are indeed same as their substrate terminations, giving an
242 8 u.c. of CTO films. We also notice that there is a weak electron density distribution above the
243 outermost CTO layers. This suggests that there are incomplete atomic layers arising from the
244 small imperfections during the growth control.

245 We also performed annular bright field (ABF) STEM on (110) pseudocubic zone axis on the
246 three systems. However, we notice the topmost 1-2 u.c. of CTO films can be easily amorphized
247 by the gold deposition on top of the film during the sample preparation process, which is
248 intended for eliminating the charging effect of the electron beam. Thus, the termination of the
249 CTO films cannot be revealed by STEM, as shown in Supplementary Figure 12.

250



251

252 **Supplementary Figure 11 | (110) slices of electron densities for three systems. (110)**

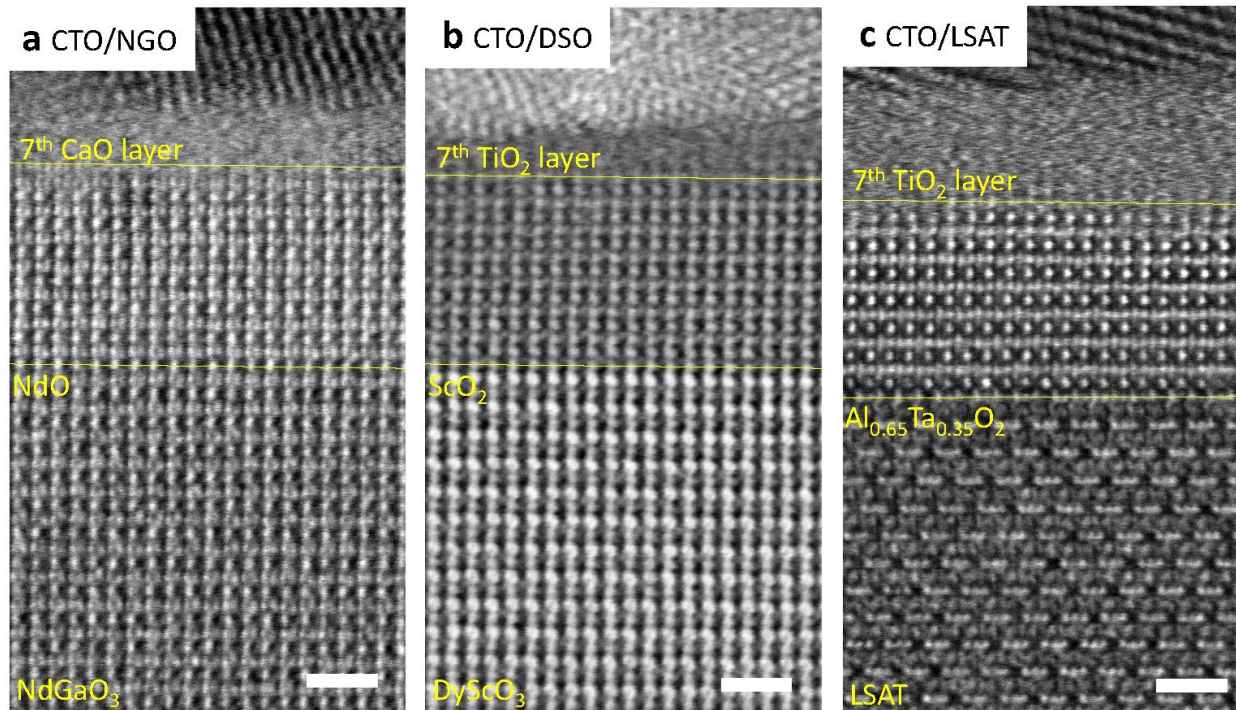
253 pseudocubic planes of coherent Bragg rods analysis (COBRA) reconstructed electron densities

254 for **a** CTO/NGO **b** CTO/DSO and **c** CTO/DSO. Alternating AO and BO₂ layers can be clearly

255 seen in this slice. These CaTiO₃ films have same terminating layer as their substrate, which

256 indicates film thickness of 8 u.c.. The scale bars are 5 Å.

257



258

259 **Supplementary Figure 12 | [110]-zone axis ABF-STEM images for three systems. [110]**

260 pseudocubic zone axis of annular bright field scanning transmission electron microscopy (ABF-

261 STEM) images for **a** CTO/NGO **b** CTO/DSO and **c** CTO/DSO. The top most 1-2 u.c. of CTO

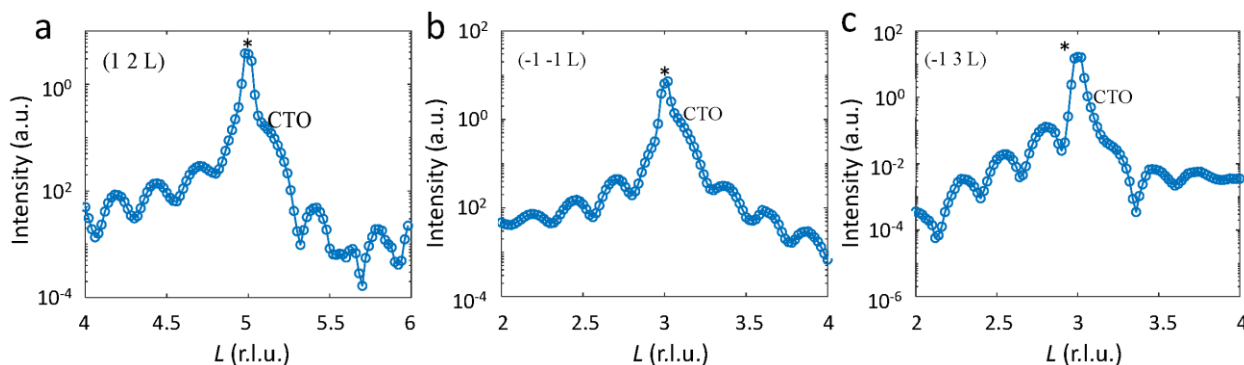
262 layers are amorphized during the gold deposition process. The scale bars are 1 nm.

263 **Supplementary Note 8: Discussion on initial model for COBRA iteration**

264 In this note, we demonstrate that the final extracted angles are not sensitive to the initial model
265 and the fits. The analysis process is detailed as following and demonstrated by the analysis on
266 the data of CTO/NGO at 30 K.

267 First, we construct an initial model of CTO film with correct tilt pattern ($a^-b^+c^-$). This can be
268 done by analyzing the half order peaks adopting the method discussed in Supplementary Note 3.
269 As shown in Supplementary Figure 13, the combination of (1 2 5), (-1 -1 3), and (-1 3 3) peaks
270 (under $2\times 2\times 2$ pseudocubic notation) from CaTiO_3 clearly indicate a tilt pattern of $a^-b^+c^-$ for
271 CaTiO_3 film on NdGaO_3 substrate.

272



273

274 **Supplementary Figure 13 | Half order peaks of CTO/NGO under $2\times 2\times 2$ pseudocubic**

275 **notation. a** The presence of (1 2 5) peak from CaTiO_3 (CTO) film indicates an in-phase tilt

276 about b -axis (b^+). The asterisk (*) marks the NdGaO_3 (NGO) substrate peak position. **b** The (-1 -

277 1 3) peak of CTO film suggests either a^- tilt or b^- tilt. Since the tilt about b -axis has been

278 determined to be b^+ , the tilt about a -axis is out-of-phase (a^-). **c** Similarly, the (-1 3 3) peak from

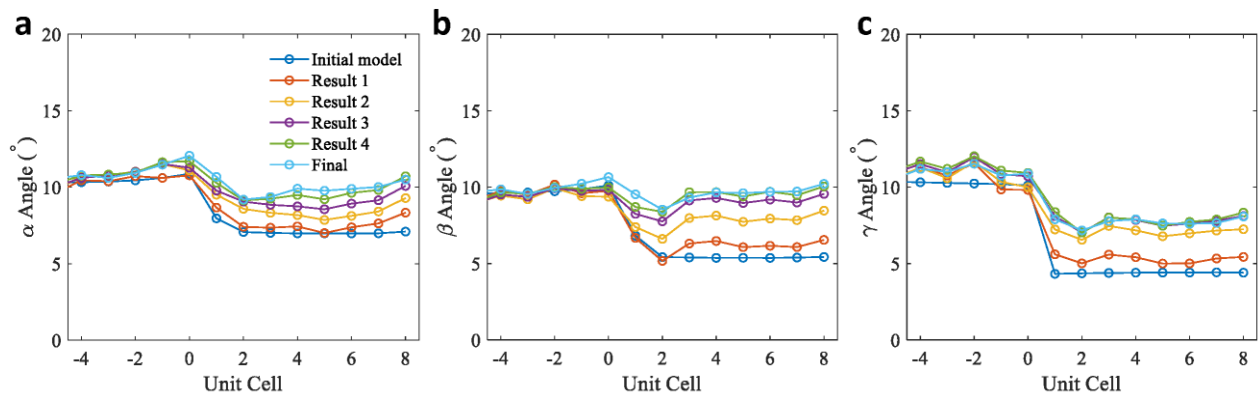
279 CTO suggests a c^- tilt about c -axis.

280

281 Then, we can choose different values for the three tilts angles of CTO. In this step, there is
282 freedom in the choice of the angles. The analysis presented in the main text used bulk tilt angles
283 of CTO as the starting point. Here, to demonstrate that the final results are not sensitive to the
284 initial tilt angles, we used a different initial model with tilt angles of 7° , 5° , and 4° respectively
285 for α , β , and γ . To overcome the stagnation during the COBRA iterations, we applied an
286 atomicity constraint, which is to remove the unphysical features in the electron densities after
287 every 10-20 iterations. The atomicity constraint was applied manually by constructing a new
288 initial model for future iterations based on the atom positions yielded from previous iterations.³
289 This process can be repeated multiple times until the results converge. Supplementary Figure 14
290 shows the tilts angles of all the intermediate states during the analysis on CTO/NGO. The
291 COBRA analysis started with the initial model of 7° , 5° , and 4° respectively for α , β , and γ ,
292 producing an intermediate tilt state shown by Result 1 in Supplementary Figure 14. Then, we
293 parameterized the atoms positions from the electron density of Result 1 and constructed a new
294 starting model for the next 10-20 iterations, which produced Result 2, etc. After repeating this
295 process for four times, the analysis converged to Result 4. As we can see in Supplementary
296 Figure 14, the tilt angles yielded by these results are very close to the results presented in main
297 Fig. 3a, which is labeled as Final in Supplementary Fig. 14.

298 These COBRA results can also be partially complemented by STEM study. As shown in main
299 Fig. 4, the COBRA yielded β angles are consistent with the STEM results. This further supports
300 the validity of the COBRA analysis.

301



302

303 **Supplementary Figure 14 | Test COBRA results with different initial model. a α , b β , and c**

304 γ values for all the intermediate states during the coherent Bragg rods analysis (COBRA) with

305 initial model of 7° , 5° , and 4° respectively for α , β , and γ . The atomicity constraint was applied

306 every 10-20 COBRA iterations to help the convergence of the results. The tilt angles given by

307 Result 4 is considerably close to the results presented in the main text (labeled as Final),

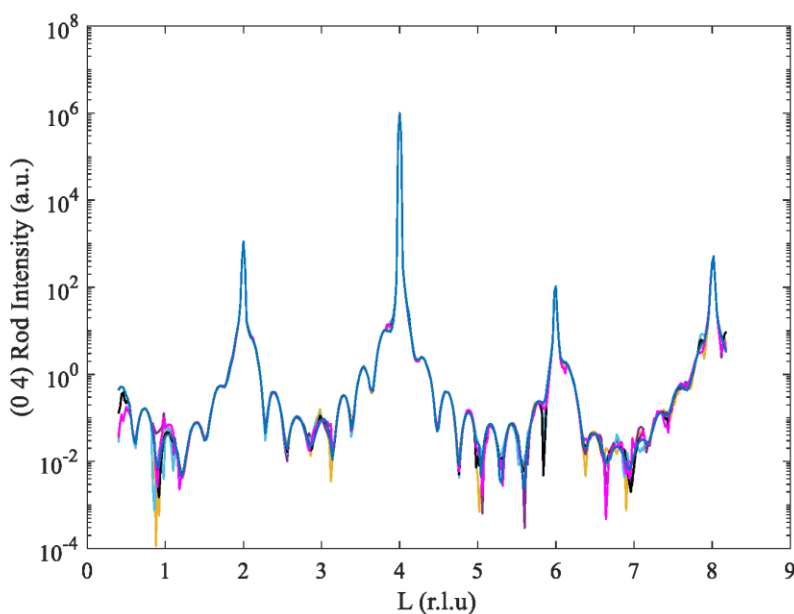
308 suggesting the COBRA results are robust towards different initial model.

309 **Supplementary Note 9: Discussion on uncertainty analysis**

310 To summarize this note, our method of error analysis (as detailed below) is more conservative
311 that Zhou's method⁴ (also described below).

312 We demonstrate this by comparing the uncertainties given by the above two methods for the case
313 of CTO/NGO at 30 K. We first construct 8 sets of CTR data (Supplementary Figure 15) with
314 simulated random noise adopting the method proposed by Zhou et al.⁴, as shown in the plot
315 below for (0 4) rod.

316



317

318 **Supplementary Figure 15 | An example of crystal truncation rod with simulated noise. (0 4)**

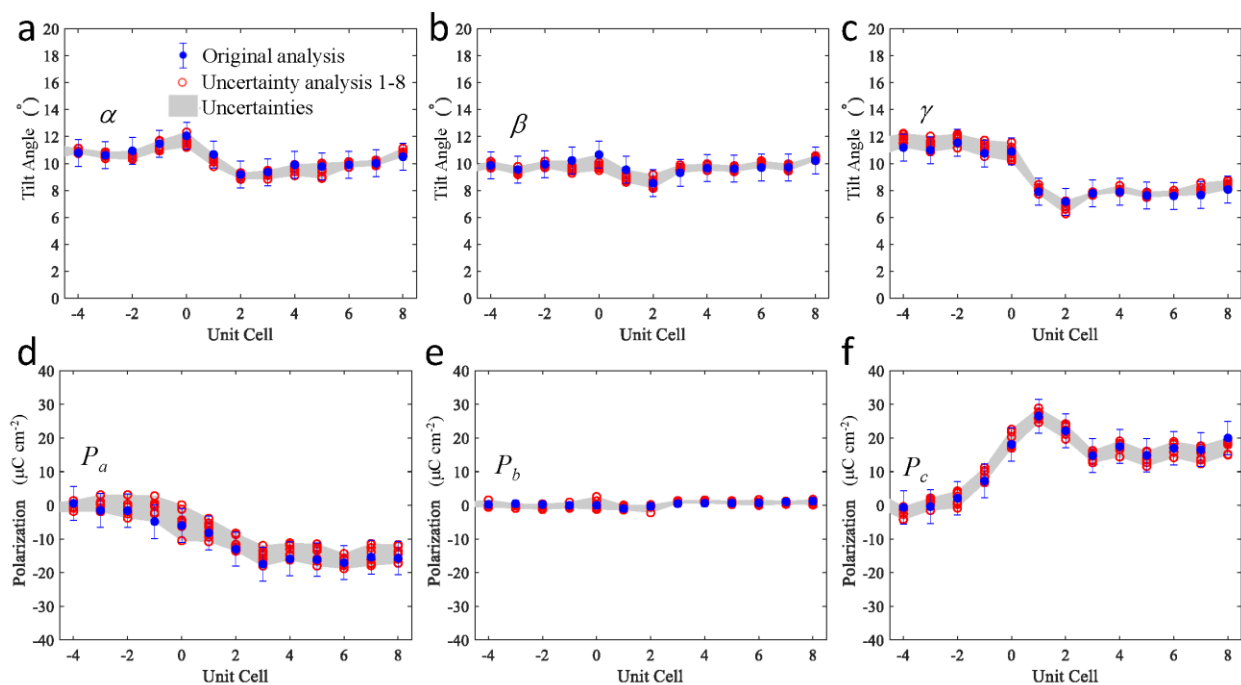
319 crystal truncation rod of CaTiO₃/NdGaO₃ with 8 different sets of simulated noise are plotted as
320 an example. The blue line is the original experimental measured (0 4) rod. Other colored lines
321 are (0 4) rod with different set of simulated noise.

322

323 The COBRA results on these 8 sets of CTR data are plotted in the figure below (Supplementary
 324 Figure 16), where blue dots and their error bars are the results from the original experimental
 325 data and simplified uncertainties estimation proposed by this work. The red open circles are
 326 results based on 8 sets of CTR data with simulated noise. The grey area presents the statistical
 327 uncertainties of all the 8 data sets.

328 We can conclude that the uncertainties given by our simplified method provide an excellent
 329 conservative estimation of the upper limits of uncertainty in the COBRA results.

330



331

332 **Supplementary Figure 16 | Comparison between two approaches of uncertainty analysis.**

333 Uncertainty analysis on $\text{CaTiO}_3/\text{NdGaO}_3$ at 30 K based on Zhou's bootstrap approach is plotted
 334 for tilt angles and polarizations using red open circles. The grey area represents the uncertainties
 335 determined from the scattering of the red open circles. The blue dots with error bars are original
 336 results using a simplified uncertainty estimation based on comparing the values for NdGaO_3 far

337 beneath the film-substrate interfaces with its bulk reference values. The blue error bars are close
338 to the upper limit of uncertainties from bootstrap approach throughout the entire thickness.

339

340 More details on Zhou's bootstrap approach and our approach are discussed as follows. Since
341 COBRA uses an iterative algorithm to reconstruct the real space electron density, traditional
342 uncertainty analysis for fitting process, that based on a parameterized numerical model, is not
343 applicable. Previously, Zhou et al, proposed a method based on the bootstrap approach to
344 estimate the uncertainty of COBRA results. In their method, experimental CTR data are first
345 randomly perturbed by simulated noise functions, and then analyzed by the COBRA method,
346 yielding a new set of real space results. This process can be repeated for multiple times, which
347 generates multiple sets of real space results. Finally, the uncertainties can be estimated by the
348 scattering extent of these sets of results. This method is a systematic way of determining
349 COBRA results' uncertainties, however, repeating COBRA iterations for a large number of times
350 to gain statistics can be extremely time and effort consuming, especially for low symmetry
351 systems of complex oxides, where a large unit cell and a large number of inequivalent atoms are
352 involved. For example, in the cases of CTO/NGO and CTO/DSO presented by this work,
353 positions of more than 350 atoms in 3D are needed for each analysis. Performing uncertainty
354 analysis for all three systems at both room temperature and 30 K using the above bootstrap
355 approach can be formidable.

356 Here we propose a straightforward way of estimating uncertainty as described in Method section.
357 The deviation of atoms positions from bulk values in the first several unit cells in the substrate
358 that are far beneath the substrate-film interfaces (> 5 u.c.) can be used as an estimation of
359 uncertainties in COBRA analysis. Although this method gives an efficient way of estimating the

360 uncertainty, it might not reflect the fact that uncertainties may vary as going from substrate to
361 film surface. Our analysis above indicates that this method is more conservative than Zhou's
362 bootstrap method.

363 **Supplementary References**

- 364 1. Biegalski, M. D. *et al.* Impact of symmetry on the ferroelectric properties of CaTiO₃ thin
365 films. *Appl. Phys. Lett.* **106**, 162904 (2015).
- 366 2. He, Q. *et al.* Towards 3D Mapping of BO₆ Octahedron Rotations at Perovskite
367 Heterointerfaces, Unit Cell by Unit Cell. *ACS Nano* **9**, 8412–8419 (2015).
- 368 3. Fong, D. D. *et al.* Direct structural determination in ultrathin ferroelectric films by
369 analysis of synchrotron x-ray scattering measurements. *Phys. Rev. B - Condens. Matter*
370 *Mater. Phys.* **71**, 1–11 (2005).
- 371 4. Zhou, H., Pindak, R., Clarke, R., Steinberg, D. M. & Yacoby, Y. The limits of ultrahigh-
372 resolution x-ray mapping: estimating uncertainties in thin-film and interface structures
373 determined by phase retrieval methods. *J. Phys. D. Appl. Phys.* **45**, 195302 (2012).

374